University of Stavanger

FACULTY OF SCIENCE AND TECHNOLOGY

MASTER'S THESIS

Study program/Specialization: Petroleum Engineering / Well Engineering	Spring semester, 2017 Open
Author: Kenny Berntsen	…… (signature of author)
Faculty supervisor: Jan Aage Aasen	
Thesis title: Experimental Design and Setup of Circulation Flow Loop - Using Particle Image Velocimetry	
Credits (ECTS): 30	
Key words: Particle image velocimetry Bingham plastic Slot configuration Velocity profile Circulation efficiency	Pages: 91 Stavanger, 25/7/2017

Master's Thesis

Experimental Design and Setup of Circulation Flow Loop - Using Particle Image Velocimetry

Kenny Berntsen

Faculty of Science and Technology
University of Stavanger

This thesis is submitted for the degree of
Master of Science

July 2017

Acknowledgements

I would like to thank my supervisor Professor Jan Aage Aasen for not only his excellent guidance when writing this thesis, but also for the many enjoyable conversations. In addition, I would like to thank both Shreyansh Divyankar and Jan Aage Aasen for letting me be a part of this interesting research project.

I would also like to thank close family and friends for supporting me through this process.

Abstract

Mud left static in a well over a longer period of time can begin to gel up or form filter cakes along the formation wall and in washout zones, which can be difficult to remove. Therefore, proper mud mobilization and removal is necessary to ensure a good zonal isolation prior to primary cementing.

The Bingham plastic rheology model is widely used by mud engineers to mathematically describe the rheological behavior of drilling fluids. The equation for circulation efficiency is directly related to the fluid velocity profile equations.

Relevant theory is introduced before experimentation and results are presented. The experimental work in this thesis is based on a field size mud conditioning operation. The annular geometry between a $9^{5/8}$-in casing and a $12^{1/4}$-in borehole is scaled down to laboratory size and configured as a slot for experimental purposes. Accompanying mud rheology and conditioning pump rate is scaled down by the Bingham number similarity method.

Particle image velocimetry (PIV) experiments were conducted on an acrylic flow channel for a Newtonian fluid to study the velocity profile. An aspect ratio of 1:10 was found to be acceptable to neglect the sidewall effects when measuring the velocity profile 8,5 centimeters from the wall, both from theoretical solutions and by comparing with experimental results.

Carbopol dispersed in an aqueous solution was found to be the most promising yield stress fluid for the future non-Newtonian PIV experiments. Despite being described better by the Herschel-Bulkley rheology model rather than the Bingham plastic model, its rheology was found to be acceptable by comparing the velocity profiles generated by the regression parameters by the two rheology models

Both analytical solutions and MATLAB were used to verify the aspect ratio and feasibility of moving on with Carbopol.

Table of Contents

List of Figures

Abbreviations

CCD	-	Charged Coupled Device
CCIR	-	Consultative Committee for International Radio
CDI	-	Central Difference Interrogation
CLAHE	-	Contrast Limited Adaptive Histogram Equalization
CMOS	-	Complementary Metal Oxide Semiconductor
CMC	-	Carboxymethyl Cellulose
CSR	-	Controlled Shear Stress
CSS	-	Controlled Shear Stress
DPGL	-	Diode Pumped Green Laser
EC	-	Electronically Controlled
FDI	-	Forward Difference Interrogation
FFT	-	Fast Fourier Transform
FPP	-	Fluorescent Polymer Particles
GUI	-	Graphical User Interface
HB	-	Herschel Bulkley
HGS	-	Hollow Glass Spheres
HSE	-	Health, safety and Environment
ID	-	Inner Diameter
MCR	-	Modular Compact Rheometer
Nd: YAG	-	Neodymium Yttrium Aluminum Garnet
OD	-	Outer Diameter
PAC	-	Polyanionic Cellulose
PIV	-	Particle Image Velocimetry

PSP	-	Polyamide Seeding Particles
PV	-	Plastic Viscosity
RPM	-	Rotations Per Minute
XG	-	Xanthan Gum
YP	-	Yield Point

Nomenclature

A	-	Area
d_i	-	Inner diameter
d_o	-	Outer diameter
F	-	Force
g	-	Gravitational force
h	-	Height
p	-	Pressure
Q	-	Flowrate
q_D	-	Dimensionless flowrate
u	-	Velocity in x-direction
u_d	-	Dimensionless velocity
v	-	Velocity in y-direction
w	-	Velocity in z-direction
y	-	Arbitrary distance along y-axis
y_D	-	Dimensionless y
η	-	Circulation efficiency
γ	-	Shear rate
θ	-	Dial reading
ρ	-	Density
σ	-	Normal stress
τ	-	Shear stress
τ_D	-	Dimensionless shear stress

τ_0	-	Shear stress at wall

1 Introduction

Studying mud conditioning by investigating fluid velocity profiles in the sheared and unsheared regions can reveal information used to optimize mud circulation and displacement efficiency. Achieving mud mobilization is crucial when performing a mud conditioning operation. Excess mud on the formation wall, in washout zones and other cavities can contaminate the cement and weaken the integrity of the well, which will lead to remedial cement operations.

The work presented in this thesis is part of a larger research, which spans over a greater amount of time than what was given to write this report. The final and concluding results of this study will be presented in the SPE paper [1].

The main objectives in this thesis is presented in the three following points:

- Design and construct a laboratory sized flow loop to represent the concentric annulus of a field size mud conditioning operation.
- Identify a transparent yield stress fluid for PIV experiments to simulate mud at laboratory conditions.
- Verify analytically and experimentally an acceptable dimension aspect ratio such that the velocity profile in the center of the channel would match that of an infinite wide duct.

2 Primary Cementing and Mud Conditioning

2.1 Primary Cementing

The process of primary cementing involves placing cement in the annulus between the casing and formation. The goal is to provide and maintain a zonal isolation from water, oil and gas bearing zones. In order to prevent fluid channels occurring in the cement sheath, a hydraulic seal must be formed between the casing and the cement, and between the cement and formations. In the absence of a complete isolation in a well, it may not reach its full producing potential [2].

Several aspects to the success of a well relies on the accomplishment of the primary cement operation. The zonal isolation does not directly relate to production, however, it plays a crucial role in how efficiently a well can be produced and stimulated. Even though the main objective is to isolate the well from formation fluids, primary cementing can also [3]:

- Prevent kicks from migrating
- Prevent blowout situations
- Seal of thief and lost circulation zones
- Support the load of the casing string
- Protect the casing from corrosion

The two-plug method for pumping and displacement is the most common way to perform a primary cement operation. When target depth is reached, the drill pipe is removed and a string of casing is run down the hole. This is carried out while mud is still in the wellbore. The mud must then be removed and replaced by cement slurry in order to accomplish a successfully primary cement job.

The two-plug method prevents the mud from contaminating the cement slurry as it is pumped down the wellbore. When the casing has been landed, a spacer and washer fluid is pumped down the wellbore followed by a pre-measured volume of cement and the displacing mud. The volume of cement is pumped up through the annular void between the casing and formation to at least the top of the productive zone. The cement is allowed to set before it is tagged and pressure tested. Depending on which section that has been cemented, the well is either further drilled or completed [4].

The success of a cement operation is dependent on the condition of the wellbore. Washout zones and out of gauge zones, which are caused by either soft or unconsolidated formations can pose

obstacles. Washout zones will result in an irregular wellbore geometry which can be difficult to clean out. Stationary mud can gel up or dehydrate in these cavities and end up contaminating the cement slurry. A thoroughly planned, designed and executed primary cement operation will ensure primary well barrier integrity and will reduce the need for a remedial cementing operation. This will lower operation and maintenance costs and furthermore increase the chances of meeting the requirements within [3]:

- Economy
- Liability
- Safety
- Government regulations

2.2 Mud Removal

Mud removal has been a subject of great interest since the 1940s. It has an important impact on the cement quality and zonal isolation during a cement operation. Execution of sufficient removal of drilling mud and preflushes are essential to ensure a good primary cement operation. Mud contamination of the cement can alter its rheology to undesirable properties. Poor mud displacement can leave behind mud channels and mud layers on the wall leading to bad cement bonding and resulting in interzonal communication.

Although the fundamentals in displacing mud to mud and mud to completion fluid are very similar to displacing mud to cement, the means and goals are somewhat different. The main stages of preparation lie behind ensuring a concentric casing placement, calculating the right cement volume and determining the correct rheological properties. Casing centralization has a mentionable effect on optimizing the mud removal.

Mud conditioning can be explained as circulating the well before and while the drill string is being pulled out of the well. As the drill string is completely out of the well, circulation stops leaving the mud static. Circulation of mud resumes during lowering of the casing. When the casing has landed, the mud is displaced and cement pumping and placement begins.

Investigated as early as 1940, Jones and Berdine [5] showed that poor zonal isolation could contribute to channeling of the cement slurry through the mud. This phenomenon was found to be promoted by casing eccentricity. Insufficient mud displacement could also lead to residual mud filter cakes at the cement to formation interface.

For several years theoretical, experimental and field studies have been carried out to further understand mud displacement. However, both experimental and theoretical approaches to this understanding have severe limitations. One laboratory limitation is the reproduction of the casing length to annular gap ratio. This parameter can reach an order of magnitude of 10^4 in the field, while in the laboratory one is typically limited to a ratio of around 500. Another limitation is with respect to the number of parameters involved. Extensive amount of work awaits one that would want to experimentally investigate the displacement efficiency of the complete dimensionless parameter space. With the above mentioned taken into account, one must be cautious when extrapolating experimental values outside of the domain of which they were acquired.

Published material of experimental studies on fluid displacement is limited. Theoretical approaches to mud displacement have its own limitations regarding rheology, unsteady momentum and mass transfer between different fluids in an irregular geometry. Several two- and three-dimensional models for annular representation do exist, however, computational power still limits the three-dimensional models. Many of the important parameters such as chemical interaction and filter cake deposition is still difficult to model. Several models does not take into consideration that interfacial mixing occurs. In other words, many models assume a clean separation between the fluid interfaces. Modelling interfacial instabilities due to differences in viscosity or density are still at an early stage.

As of today, there exists no direct method of measuring the efficiency of mud removal. Even though the accuracy of prediction is still limited, progress has been achieved during the past decade by combining experimental studies and theoretical approaches. The effect of casing movement, mixing of fluids and unsteady flow are technical challenges that need better quantification. The success of a cement operation is difficult to quantify for reasons such as [6]:

- Monitoring of a field cement operation exhibits several differences as compared to laboratory experiments.
- The wellbore condition is often partly unknown.
- The laboratory mixed fluids can be very different from the fluids mixed in the field.

2.3 Well Preparation

Correct centralization of the casing string can be difficult in a well with large angles and dogleg sections with high severity. This may result in complications while removing mud from the narrow side of the annulus. Washout zones, filter cakes and settled cutting beds can be

problematic or nearly impossible to clean out. The mud may contaminate the cement slurry as washout zones often tend to contain gelled or dehydrated mud. The main objective of a drilling engineer is to reach target depth as safely, quickly and economically as possible, however, it should be done while providing an optimal wellbore for later operations, such as cementing or completion. An acceptable wellbore condition is attained if it fulfills the characteristics listed below:

- Controlled wellbore pressures
- A smooth wall with mild dogleg severities
- In-gauge borehole
- Absence of cutting beds
- Properly conditioned and mobile mud that will leave a thin filter cake at permeable zones

Static situations over a longer period of time can result in thick filter cakes and weight material settling, which are hard to remove and can complicate the operation of running a casing. A caliper or survey log can also misinterpret the out of gauge hole due to a thick filter cake [7].

2.4 Mud Conditioning

Due to the fact that drilling muds primarily are designed to aid during drilling operations, it is necessary to alter its properties prior to the cement operation. In order to increase the mobility of the mud, it is often desirable to reduce the mud density, gel strength, yield strength and plastic viscosity. It is regular procedure to circulate the annular volume at least once to clean and modify the rheology of the mud. Once the mud has obtained its necessary rheological properties, the drill pipe can be removed from the borehole. If the mud is not conditioned correctly, this can lead to mud gelling which is difficult to remove. Mobilization and rotation of the drill string during mud conditioning will assist the displacement of gelled mud and keep cuttings in suspension. It is advantageous to circulate the mud prior to cementation as it will:

- Aid in cuttings transportation.
- Investigate if there are any occurrences of gas flow in the well.
- Ensure post treatment homogenizing of the mud
- Ensure desirable rheological properties as must muds are time dependent.
- Mobilize gelled or dehydrated mud that has settled in washout zones or on the narrow side of the eccentric placed casing.

A great amount of pressure buildup can occur after circulation is resumed as cuttings, gelled or dehydrated mud are scraped off the wall

For a laminar flow in a concentric annulus, the circulation efficiency of a Bingham plastic fluid can approximated by the following equation:

$$\eta = \frac{12\bar{u}}{d_o - d_i}\left(\frac{\mu_p}{\tau_y}\right) \tag{2.1}$$

Where d_o and d_i denotes the outer and inner diameter of the annulus, respectively. The average velocity is presented as $\bar{u}$, while μ_p and τ_y is the plastic viscosity and the yield point of the Bingham plastic fluid [8]. When the Bingham plastic equations are presented in chapter 3.7.3, it can be seen that the circulation efficiency equation (2.1) is directly related to the velocity profile of the Bingham plastic fluid.

3 Hydraulic Models

3.1 Rheology

The word rheology originates from the Greek language and is translated to “The study of flow”. This field of study describes the flow and deformation of matter, primarily liquids and soft solids, which behave in plastic flow. However, rheological measurements can be applied to all materials, liquid, solids and gas. Materials, usually solids, which deform elastically in respond to an applied force, may be best described otherwise. Rheology provides a great deal of information regarding the relationship between deformation, forces and time. The science of rheology is of relevance in a number of disciplines and industries from the petroleum industry to chemistry and biology.

Rheology is especially of importance to the petroleum industry. When studying fluids properties, one can better understand and predict how drilling mud and production fluids will behave under different pressures and temperatures [9].

Part of the theory included from chapter 3.1 to 3.6 is based upon the Bachelor’s thesis [60], where different rheology models were investigated.

3.2 Viscosity

Together with density, viscosity is one of the most important parameters of a fluid. Viscosity is a measurement of the fluids resistance to flow. The flow resistance can occur due to different factors. Some of them are listed below.

- Frictional forces between the particles in the fluid
- Intermolecular and intramolecular forces between electrical charged particles and ions in the fluid

Several parameters govern the viscosity, such as [10]:

- Temperature
- Pressure
- Time
- Shear rate
- Physical and chemical composition of the fluid

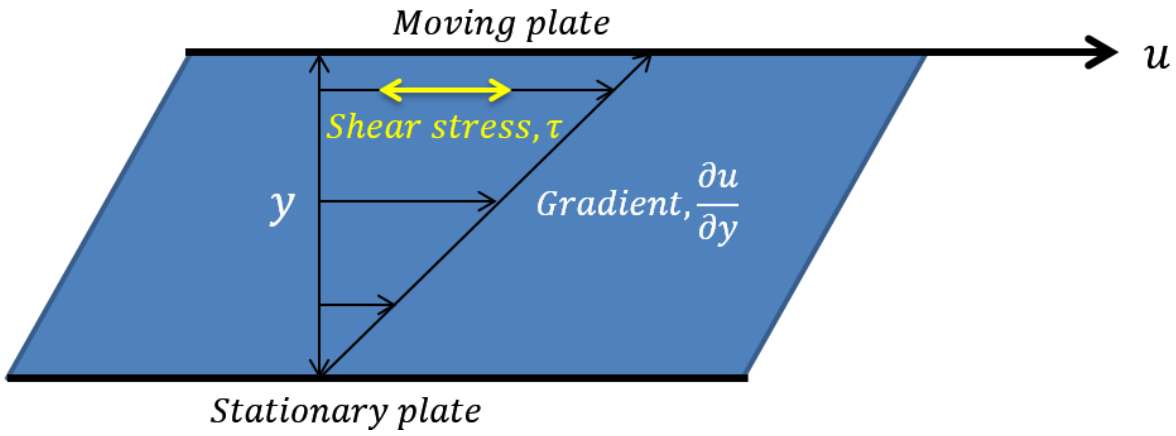

Figure 3.1: Flow of a viscous fluid between plates [60].

Two boundary plates, covering a total area of A with a fluid in between, is considered. The bottom boundary plate is stationary, while the top boundary plate is moving in a horizontal direction at a constant velocity. The fluid is in contact with both plates. The end effects are not considered since the boundary plates are assumed to be infinitely long. The distance between the plates is considered as *y*. If the top boundary plate is moving at a small enough velocity, the fluid particles are assumed to move parallel to it, which means that the velocity will increase linearly form zero at bottom to *v* at the top. The friction between the fluid layers will give raise to a force *F*, resisting their relative motion.

The following equation gives the shear stress:

$$\tau = \frac{F}{A} \tag{3.1}$$

The shear rate is usually measured in s^{-1} and given by equation (3.2):

$$\gamma = \frac{dv}{y} \tag{3.2}$$

The viscosity can be measured in N s/ m^2 = Pa.s and is given by equation (3.3):

$$\mu = \frac{\tau}{\gamma} \tag{3.3}$$

The ratio du/dv is the derivative of the fluid speed perpendicular to the boundary plates and is known as the rate of shear deformation. The force *F* can be expressed to be proportional to the velocity *u* and the area *A* of each of the boundary plates, and inversely proportional to the distance between the boundary plates, *y*, as shown in equation (3.4):

$$F = \mu A \frac{u}{\gamma} \tag{3.4}$$

The viscous forces of a fluid can also be expressed by the following differential equation:

$$\tau = \mu \frac{\partial u}{\partial y} \tag{3.5}$$

3.3 Rheometer

There are several ways to measure the viscosity of a fluid. The use of a rheometer is most common way. A rheometer is a laboratory apparatus used to determine the relationship between the shear rate and shear stress in a fluid, but also several other fluid characteristics. The liquid viscosity may also vary with flow conditions.

The concept from figure 3.1 can also be applied to a cylinder, which is shown in figure 3.2.

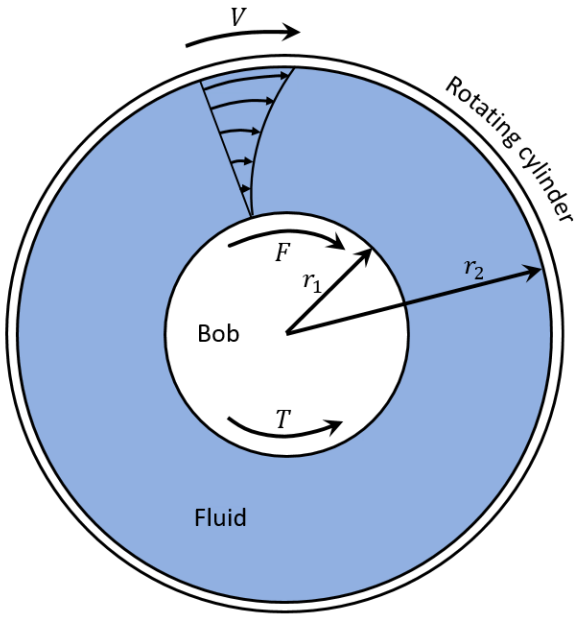

Figure 3.2: Flow of a viscous fluid in a cylinder [60].

The setup consists of an inner stationary cylinder, surrounded by the fluid in testing and completed by an outer, rotating cylinder. When rotating the outer cylinder, the inner cylinder will, as discussed in chapter 3.2 experience a force *F*, due to the friction between the fluid layers.

3.3.1 Fann Viscometer (Fann VG 35) and OFITE Model 800 Viscometer

The Fann VG 35 Viscometer and OFITE Model 800 Viscometer were used during the fluid design which is further described in chapter 5.2. The two viscometers are similar in structure and functionality. What differs one from the other is the choices of rotation speeds and the gear mechanisms

The OFITE also offers a magnification glass and light at the place of dial reading and is considered to be more accurate.

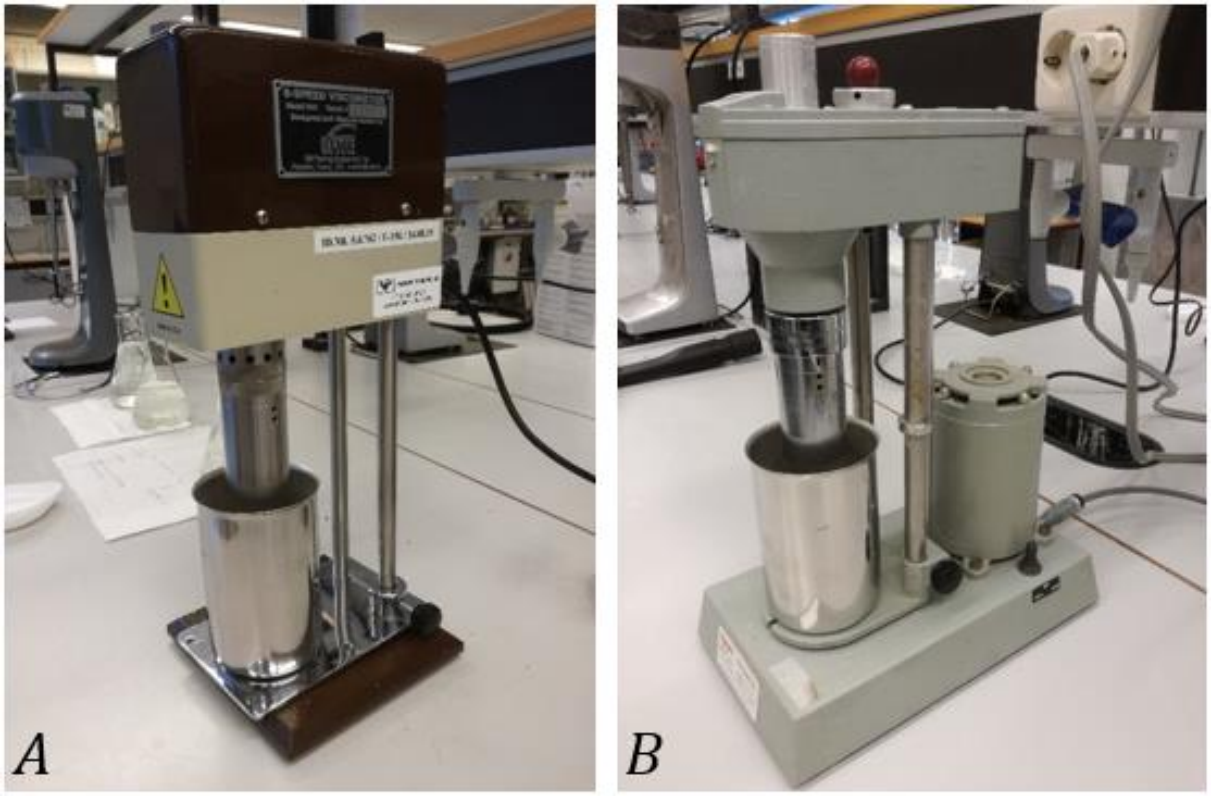

Figure 3.3: A) OFITE Model 800 Viscometer and B) Fann VG 35 Viscometer.

This type of equipment consists of an inner cylinder (bob) which is suspended by a torsion spring. The apparatus is built on the concept illustrated in figure 3.2. When the outer cylinder rotates, the fluid layer closest to the outer cylinder in the annulus will achieve approximately the same velocity as the outer cylinder. The velocity of the fluid layers will decrease when approaching the inner cylinder. The innermost fluid layer tends to drag the inner cylinder

around, and the force it exerts on this cylinder can be measured as torque. The torsion spring, which the bob is connected to, acts as a counter force. When this spring force is overcome, the inner cylinder will rotate. The dial reading (θ) that can be observed at the top of the viscometer is an expression of the liquids shear stress and can be measured in degrees.

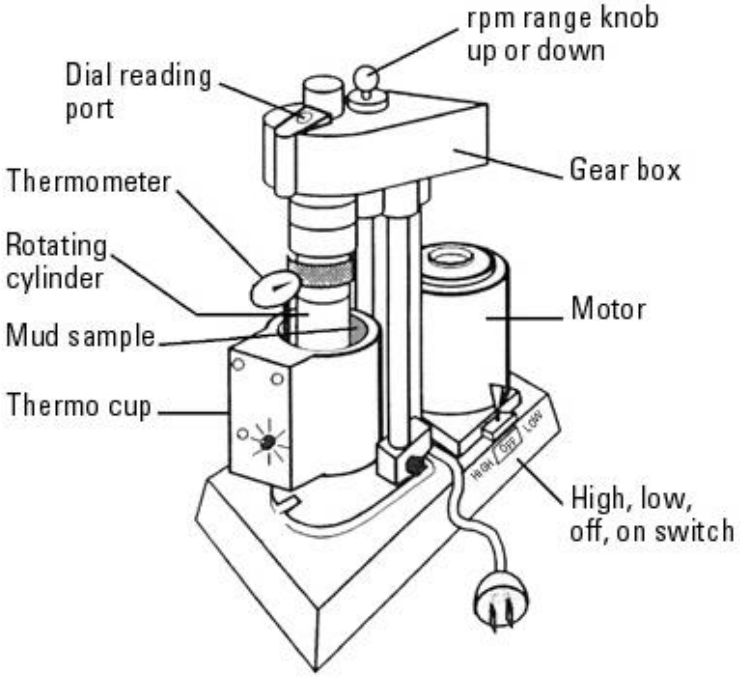

Figure 3.4: A typical field viscometer [11].

The Fann VG 35 viscometer can record dial reading at the following shear rates, 3, 6, 100, 200, 300 and 600 rotations per minute (RPM), while the OFITE Model 800 offers additional rotation speeds at 60 and 30 RPM.

According to the instruction manual for the Fann VG 35 viscometer, the shear stress can be converted to:

- lbf/100ft^2 by multiplying the dial reading by a factor of 1.067
- Dynes/cm^2 by multiplying the dial reading by a factor of 5.11
- Pa by multiplying the dial reading by a factor of 0.511

And the shear rate can be converted to:

- s^{-1} by multiplying the shear rate in RPM by a factor of 1.7023

3.3.2 Anton Paar 302 Viscometer

The Anton Paar MCR (Modular Compact Rheometer) 302 was also used during the fluid design to verify the rheological properties determined by the simpler rheometers, Fann VG 35 and OFITE Model 800. This is a much more complex designed and accurate rheometer. The upmost important component of the Anton Paar MCR 302 is its air-bearing-supported synchronous EC motor, which delivers accurate rheology measurements. The motor is equipped with magnets and coils with opposite polarity which produce magnetic poles. The rotating flux created when the magnets and coils attract each other produce a frictionless movement of the motor, which delivers precise torque and measurements. The concentric cylinder configuration explained in chapter 3.3 was also used on the Anton Paar MCR 302. A comparison of the rheological results in chapter 5.1.5 from the Fann VG 35 or OFITE and the Anton Paar MCR 302 shows overall good correlation. Two tests were done by the Anton Paar to determine the yield point of the several fluids tested. Firstly the controlled shear rate (CSR) test and later the controlled shear stress (CSS) test. The shear rate is ramped down in the CSR test, while it is ramped up in the CSS test [13].

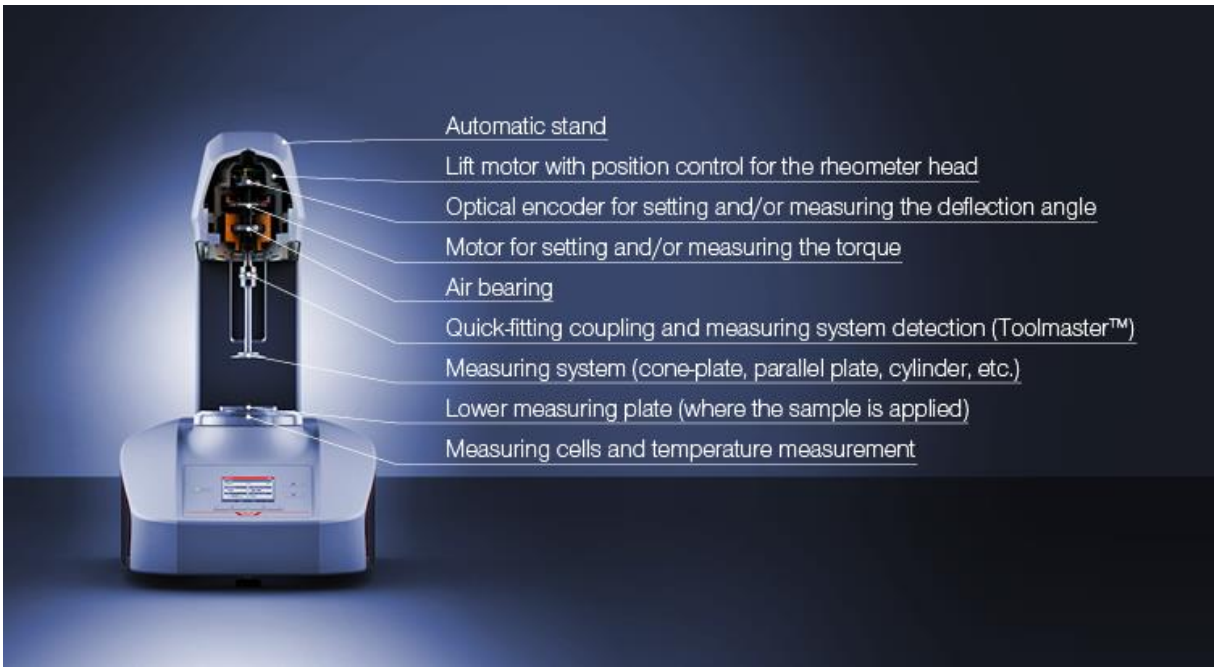

Figure 3.5: Anton Paar MCR 302 Rheometer.

3.3.2.1 Controlled Shear Rate (CSR)

The CSR test cannot measure the yield point of a fluid directly. It is calculated by fitting a function which is adapted to the measured points on the curve. Various models can be used fitting the curve, e.g. Bingham plastic or Herschel-Bulkley. The yield point is determined by extrapolating the measured points on the curve towards a shear rate value of zero. As the different rheology models are based on different calculations, they also generate a different value for the yield point [13].

3.3.2.2 Controlled Shear Stress (CSS)

This test is a commonly used method of determining the yield point of a fluid. The shear rate is ramped up with time while the shear stress is measured and taken as the yield point value if no motion in the fluid is detected. This is the last point where the shear rate is still measured to be zero. Compared to the CSR test, the CSS is a better method of measuring the yield point [13].

3.4 Rheological Parameters

The rheological properties of mud and other fluids are commonly characterized by the following properties [10]:

- **Plastic viscosity (PV)**

  Plastic viscosity (PV) is a parameter seen in the Bingham plastic rheology model. PV represents the slope above the yield point in a shear stress/shear rate diagram. This part of the fluid's flow resistance is caused by the mechanical friction between particles in the fluid, between the particles and the liquid phase and between the liquid elements themselves. PV is therefore dependent on the shape, size and concentration of the particles within the fluid.

- **Yield point (YP)**

  The yield point is also a parameter in the Bingham plastic model. This part of the flow resistance occurs due to attractive forces between the particles in the fluid as a result of electrostatic forces. On a shear stress/shear rate diagram, this parameter represents the point where the slope crosses the shear stress axis and is also where shear rate is zero.

- **Gel strength**

  The gel strength represents the fluid's thixotropic properties. When constant shear stress is applied to a fluid and left to rest for some time, the viscosity will start at an initially higher value and drop asymptotically over time to a final, lower value. The gel strength

is measured as a function of time and it is related to the attractive forces between the particles when the fluid is stationary [14].

3.5 Newtonian vs. Non-Newtonian Fluid

Fluids can in general be generalized and divided into two different groups according to their rheological properties, namely Newtonian and non-Newtonian fluids.

3.5.1 Newtonian Fluids

Newtonian fluids can be described as pure and simple in composition and containing particles smaller than the size of molecules. Water is the best example of a Newtonian fluid. Oil and glycol will also behave as a Newtonian fluid.

A Newtonian fluid is known to behave in a specific way, where the relationship between the shear stress and shear rate is linear. The coefficient of viscosity is then equal to the constant of proportionality. In other words, the size of the droplets is directly related to the thickness of the fluid, all else remaining the same [15].

$$\mu = \frac{\tau}{\gamma} \tag{3.6}$$

3.5.2 Non-Newtonian Fluids

For a non-Newtonian fluid, the relation between shear stress and shear rate in non-linear. These fluids can be shear thinning, shear thickening and thixotropic. Therefore, defining a constant of coefficient for a non-Newtonian fluid cannot be done [16].

$$\mu \neq \frac{\tau}{\gamma} \tag{3.7}$$

3.5.2.1 Bingham Plastic Rheology Model

The Bingham plastic model is named after Eugene C. Bingham and is the most common rheology model used to determine the rheology of non-Newtonian drilling fluids [17]. It is a two parameters model that include the plastic viscosity and yield point of the fluid. The model assumes that the relation between the shear stress and shear rate is a linear function above the yield point as explained in chapter 3.4 and represented in figure 3.6. The Bingham plastic rheology model can be described by the equation (3.8) [18]:

$$\tau = \tau_y + \mu_p \gamma \tag{3.8}$$

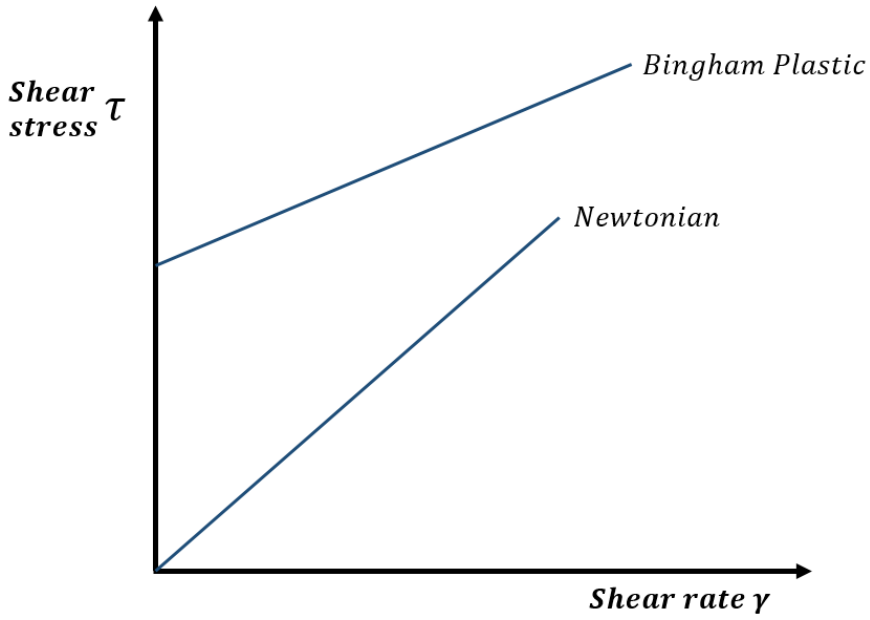

Figure 3.6: Shear rate vs. Shear stress.

3.6 Flow Regimes

Fluid flows can be classified and divided into three categories, laminar, transitional or turbulent flow regime. In the model used in this thesis, and many other rheological models, the Reynolds number determines the flow regime.

The Reynolds number is a dimensionless quantity used to predict flow patterns in a particular fluid at different velocities. The Reynolds number can also be used as a scaling quantity of similar but different sized flow investigations, such as a laboratory experiment and a full-scaled version. Laminar flow occurs when the Reynolds number is below 1000 and is characterized as a smooth and constant flow where viscous forces are dominant. The fluid will flow in streamlines parallel to each other with no disturbance between the layers. The transitional flow regime occurs for Reynolds numbers between 1000 and 2000. Turbulent flows, on the other hand occurs at Reynolds numbers over 2000. This flow regime is characterized as chaotic and is governed by the inertial properties of the fluid in motion [19].

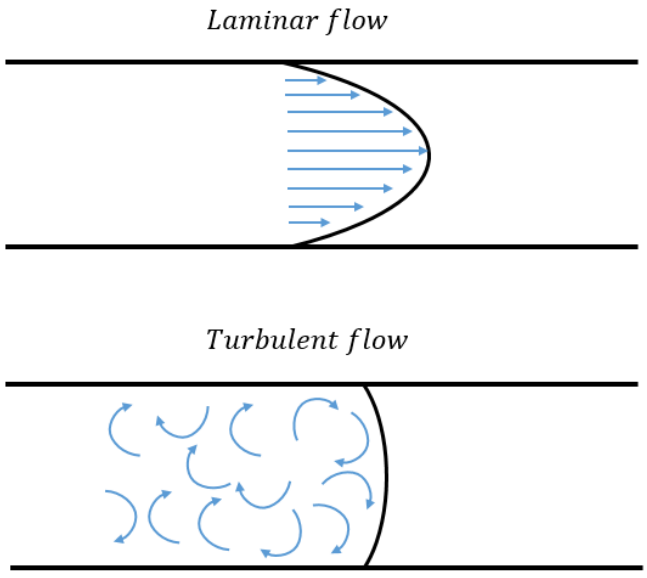

Figure 3.7: Illustration of laminar and turbulent flow regime.

3.7 Fluid Velocity Profile

3.7.1 Navier-Stokes

The Navier-Stokes equations were developed and named after Claude-Louis Navier and George Gabriel Stokes in 1822. These sets of equations were obtained by combining Newton's second law to the motion of a fluid together with the fluid stress and a pressure term to describe viscous flow. When combining the equations of motion together with the continuity equation (conservation of mass) we arrive at the Navier-Stokes equation.

The general differential equations of motion for a fluid, which are derived from the forces acting on a small cubical fluid element, can be expressed as the following [20, 21]:

$$\rho g_x + \frac{\partial \sigma_{xx}}{\partial x} + \frac{\partial \tau_{yx}}{\partial y} + \frac{\partial \tau_{zx}}{\partial z} = \rho \left(\frac{\partial u}{\partial t} + u \frac{\partial u}{\partial x} + v \frac{\partial u}{\partial y} + w \frac{\partial u}{\partial z} \right) \tag{3.9}$$

$$\rho g_y + \frac{\partial \tau_{xy}}{\partial x} + \frac{\partial \sigma_{yy}}{\partial y} + \frac{\partial \tau_{zy}}{\partial z} = \rho \left(\frac{\partial v}{\partial t} + u \frac{\partial v}{\partial x} + v \frac{\partial v}{\partial y} + w \frac{\partial v}{\partial z} \right) \tag{3.10}$$

$$\rho g_z + \frac{\partial \tau_{xz}}{\partial x} + \frac{\partial \tau_{yz}}{\partial y} + \frac{\partial \sigma_{zz}}{\partial z} = \rho \left(\frac{\partial w}{\partial t} + u \frac{\partial w}{\partial x} + v \frac{\partial w}{\partial y} + w \frac{\partial w}{\partial z} \right) \tag{3.11}$$

Where u, v, and w denotes the velocity vectors in x-, y-, and z-direction respectively.

These equations can be applied to any solid or fluid either in motion or at rest.

The continuity equation is one of the most important equations in fluid mechanics, which is valid for both steady and unsteady flow as well as compressible and incompressible fluid. It describes the conservation of mass:

$$\frac{\partial \rho}{\partial t} + \frac{\partial (\rho u)}{\partial x} + \frac{\partial (\rho v)}{\partial y} + \frac{\partial (\rho w)}{\partial z} = 0 \tag{3.12}$$

By using the continuity equation to simplify the equations of motion, we can express the Navier-Stokes equations in Cartesian coordinates:

X-direction

$$\rho\left(\frac{\partial u}{\partial t}+u\frac{\partial u}{\partial x}+v\frac{\partial u}{\partial y}+w\frac{\partial u}{\partial z}\right)=-\frac{\partial p}{\partial x}+\rho g_x+\mu\left(\frac{\partial^2 u}{\partial x^2}+\frac{\partial^2 u}{\partial y^2}+\frac{\partial^2 u}{\partial z^2}\right) \quad (3.13)$$

Y-direction

$$\rho\left(\frac{\partial v}{\partial t}+u\frac{\partial v}{\partial x}+v\frac{\partial v}{\partial y}+w\frac{\partial v}{\partial z}\right)=-\frac{\partial p}{\partial y}+\rho g_y+\mu\left(\frac{\partial^2 v}{\partial x^2}+\frac{\partial^2 v}{\partial y^2}+\frac{\partial^2 v}{\partial z^2}\right) \quad (3.14)$$

Z-direction

$$\rho\left(\frac{\partial w}{\partial t}+u\frac{\partial w}{\partial x}+v\frac{\partial w}{\partial y}+w\frac{\partial w}{\partial z}\right)=-\frac{\partial p}{\partial z}+\rho g_z+\mu\left(\frac{\partial^2 w}{\partial x^2}+\frac{\partial^2 w}{\partial y^2}+\frac{\partial^2 w}{\partial z^2}\right) \quad (3.15)$$

It is these equations from which the velocity profile equations for Newtonian fluids we know today are derived.

3.7.2 Newtonian Fluid Profile

Considering a rectangular duct with a laminar flow where the side wall effects are negligible. For this geometry, there is no velocity in the y- or z-direction, therefore $v = 0$ and $w = 0$. It follows from the continuity equation that $\partial u/\partial x$. When neglecting the side wall effects, u will not vary in the z-direction, and since we are considering a steady flow $\partial u/\partial t = 0$, so that $u = u(y)$. When taking into account these conditions, the Navier-Stokes equations reduce to:

$$0 = -\frac{\partial p}{\partial x}+\mu\left(\frac{\partial^2 u}{\partial y^2}\right) \quad (3.16)$$

Acknowledging the gravitational force in the y-direction and neglecting it in both x- and z-direction, setting $g_x = 0,\ g_z = 0$ and $g_y = -g$, the Navier-Stokes equations is simplified to:

$$0 = -\frac{\partial p}{\partial y} - \rho g \tag{3.17}$$

$$0 = -\frac{\partial p}{\partial z} \tag{3.18}$$

Integrating these will yield:

$$p = -\rho g y + f_1(x) \tag{3.19}$$

Shows that the hydrostatic pressure varies in the y-direction.

Rewriting equation (3.16) as:

$$\frac{d^2u}{dy^2} = \frac{1}{\mu}\frac{\partial p}{\partial x} \tag{3.20}$$

Integrating this equation twice will first yield:

$$\frac{du}{dy} = \frac{1}{\mu}\left(\frac{\partial p}{\partial x}\right) y + c_1 \tag{3.21}$$

And then

$$u = \frac{1}{2\mu}\left(\frac{\partial p}{\partial x}\right) y^2 + c_1 y + c_2 \tag{3.22}$$

The pressure gradient $\partial p/\partial x$ is treated as a constant since it is not a function of y, for this integration. From the defined boundary conditions, two constants c_1 and c_2, can be determined. We assume a no-slip condition along the upper and lower wall, such that $u = 0$ for $y = 0$ and $y = h$. In order for this condition to be satisfied, c_1 must be equal to 0 and

$$c_2 = -\frac{1}{2\mu}\left(\frac{\partial p}{\partial x}\right) yh \tag{3.23}$$

Finally, we arrive at the velocity equation, which is:

$$u = \frac{1}{2\mu}\left(\frac{\partial p}{\partial x}\right)(hy - y^2) \tag{3.24}$$

From equation (3.24) we can see that it yields a parabolic velocity profile. This equation is also referred to as the Poiseuille's equation.

Although the sidewall effect has previously been neglected when deriving these equations, the width w will be included when presenting the equation for flowrate. This will be made clear in chapter 5.1.2 where for the given aspect ratio of $h/w = 1/10$ and the place of measurement, $w/2$ the flow channel, can be considered as an infinite wide duct for analytical purposes.

The equation of flowrate is presented as:

$$q = udA = uwdA = \frac{1}{2\mu}\left(\frac{\partial p}{\partial x}\right)\int_0^h (hy - y^2)dy \tag{3.25}$$

Resulting in

$$q = -\frac{wh^3}{12\mu}\left(\frac{\partial p}{\partial x}\right) \tag{3.26}$$

Since the pressure is decreasing in the direction of the flow, the pressure gradient term $\partial p/\partial x$ will be negative. If we let dP_f represent the frictional pressure drop across the length dL, such that:

$$\frac{dP_f}{dL} = -\left(\frac{\partial p}{\partial x}\right)$$

Equation (3.26) can be expressed as

$$q = \frac{wh^3}{12\mu}\frac{dP_f}{dL} \tag{3.27}$$

We know from circular pipe flow that the average velocity is equal to exactly half of the maximum velocity, by integrating across the velocity profile. We can execute the same operations for a rectangular configuration. By solving equation (3.27) for dP_f/dL and inserting it in equation (3.24) for $(\partial p/\partial x)$ we find that:

$$u(y) = \frac{6q}{wh^3}(hy - y^2) \tag{3.28}$$

By derivating equation (3.28) and setting it equal to zero, we find where along the slope the maximum velocity occur.

$$u'(y) = \frac{6q}{wh^2} - \frac{12q}{wh^3}y = 0 \tag{3.29}$$

Which yields

$$y = \frac{h}{2}$$

By inserting our result into equation (3.28), we find that the maximum velocity is equal to:

$$u\left(\frac{h}{2}\right) = \frac{3}{2}\frac{q}{wh} = \frac{3}{2}\bar{u} = u_{max} \tag{3.30}$$

We see that the maximum velocity is equal to $3/2$ of the average velocity in a rectangular duct.

The laminar velocity profile of a Newtonian fluid is presented below:

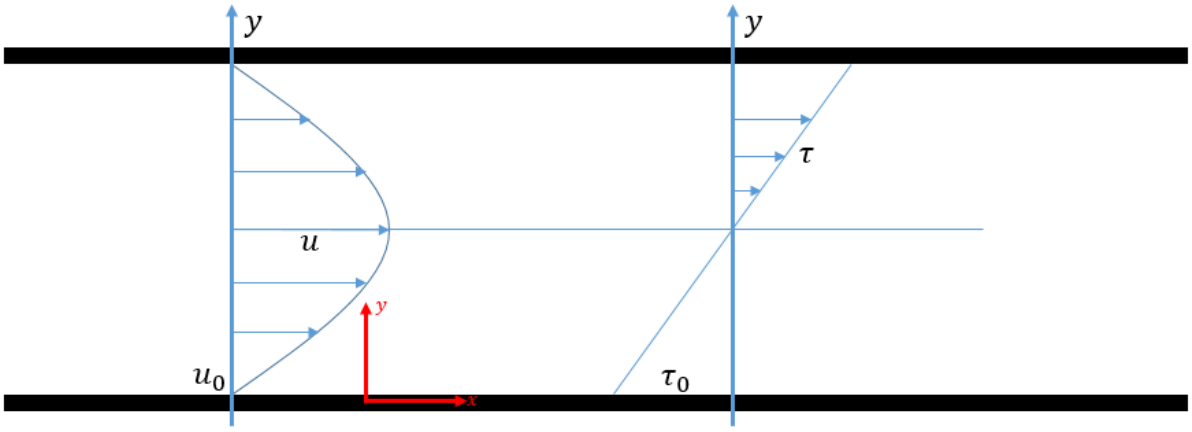

Figure 3.8: Laminar flow of a Newtonian fluid in slot.

3.7.3 Bingham Plastic Fluid Profile

For a non-Newtonian fluid, the expression of a velocity profile can be derived using the same steps as for a Newtonian fluid. In this thesis, the interest revolves around a fluid that is representable in a Bingham plastic rheology model. Deriving the flow equations for a Bingham plastic fluid is more complicated than other fluids not having a yield stress. Due to the yield stress fluid, portions of the fluid are experiencing less share rate than the yield point, which result in the middle region moving as a plug.

The velocity of a Bingham plastic fluid flowing in a rectangular duct can be expressed in three equations. First for the bottom third of the velocity profile, second for the plug region and thirdly for the upper part of the profile [22]:

$$u = \frac{1}{2\mu_p}\frac{dP_f}{dx}\left[hy\left(1-\frac{\tau_y}{\tau_0}\right)-y^2\right] \qquad \text{For } 0 \le y \le \frac{h}{2}\left(1-\frac{\tau_y}{\tau_0}\right) \quad (3.31)$$

$$u = \frac{1}{2\mu_p}\frac{dP_f}{dx}\left[hy\left(1-\frac{\tau_y}{\tau_0}\right)\right]^2 \qquad \text{For } \frac{h}{2}\left(1-\frac{\tau_y}{\tau_0}\right) \le y \le \frac{h}{2}\left(1+\frac{\tau_y}{\tau_0}\right) \quad (3.32)$$

$$u = \frac{1}{2\mu_p}\frac{dP_f}{dx}\left[(y-h)\left\{h\left(1-\frac{\tau_y}{\tau_0}\right)-(y+h)\right\}\right] \qquad \text{For } \frac{h}{2}\left(1-\frac{\tau_y}{\tau_0}\right) \le y \le h \quad (3.33)$$

The total flowrate can be found from the velocity profile equations and be expressed as:

$$q = \frac{wh^3}{12\mu_p}\frac{dP_f}{ds}\left[1 + \frac{3}{2}\left(\frac{\tau_y}{\tau_0}\right) - \frac{1}{2}\left(\frac{\tau_y}{\tau_0}\right)^3\right] \tag{3.34}$$

In figure 3.9, the velocity profile for a Bingham plastic fluid is illustrated with the patterned region representing the plug region:

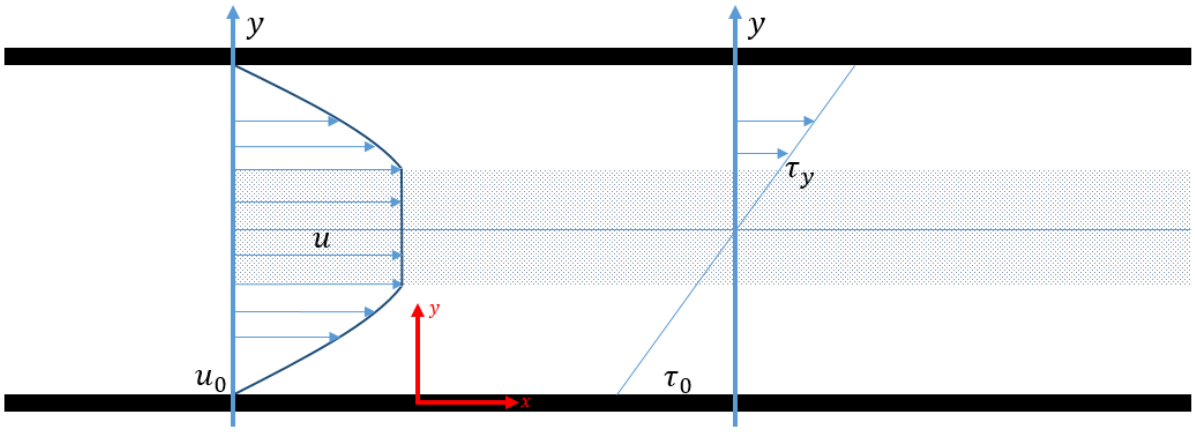

Figure 3.9: Laminar flow of a Bingham plastic fluid in slot.

3.7.3.1 Dimensionless Bingham Plastic Fluid Profile

Dimensionless parameters can be quite useful, especially when comparing with other velocity profiles. First, the dimensionless flowrate is defined. Later, the dimensionless yield point, height and bulk velocity is found.

$$q_D = \frac{q\mu_p}{wh^2\tau_y}$$

$$\frac{q\mu_p}{wh^2\tau_0} = \frac{q\mu_p}{wh^2\tau_0\frac{\tau_y}{\tau_y}} = \frac{q\mu_p}{wh^2\tau_y\frac{\tau_0}{\tau_y}} = \frac{q_D}{\frac{1}{\tau_D}}$$

Which now yields:

$$\tau_D = \frac{\tau_y}{\tau_0}, y_D = \frac{y}{h}, u_D = \frac{u}{\bar{u}}$$

Where $\overline{u}$ is the bulk velocity defined as $\overline{u} = \frac{q}{wh}$

The dimensionless velocity profile equation for the Bingham plastic rheology model can now be written as:

$$u_D = \frac{1}{q_D \tau_D} y_D[(1-\tau_D) - y_D] \qquad \text{For } 0 \leq y_D \leq \frac{(1-\tau_D)}{2} \qquad (3.35)$$

$$u_D = \frac{1}{4 q_D \tau_D}(1-\tau_D)^2 \qquad \text{For } \frac{(1-\tau_D)}{2} \leq y_D \leq \frac{(1+\tau_D)}{2} \qquad (3.36)$$

$$u_D = \frac{1}{q_D \tau_D}(y_D - 1)[(1-\tau_D) - (y_D + 1)] \qquad \text{For } \frac{(1+\tau_D)}{2} \leq y_D \leq 1 \qquad (3.37)$$

4 Particle Image Velocimetry

Particle Image Velocimetry (PIV) is a non-intrusive visualization and measurement technique in fluid mechanics used to determine instantaneous fields of the vector velocity. It is done by measuring the displacement of micro sized, neutral buoyant particles added to the fluid. These particles are assumed to accurately follow the motion of the fluid. Compared to techniques that employ probes, such as pressure tubes or other equipment for measuring flow velocity, the PIV delivers an optical method which will not disturb the flow. This allows the PIV method to be used in high-speed flows with shocks or in boundary layers close to the wall, where flow may be disturbed by the presence measuring equipment [23, 24].

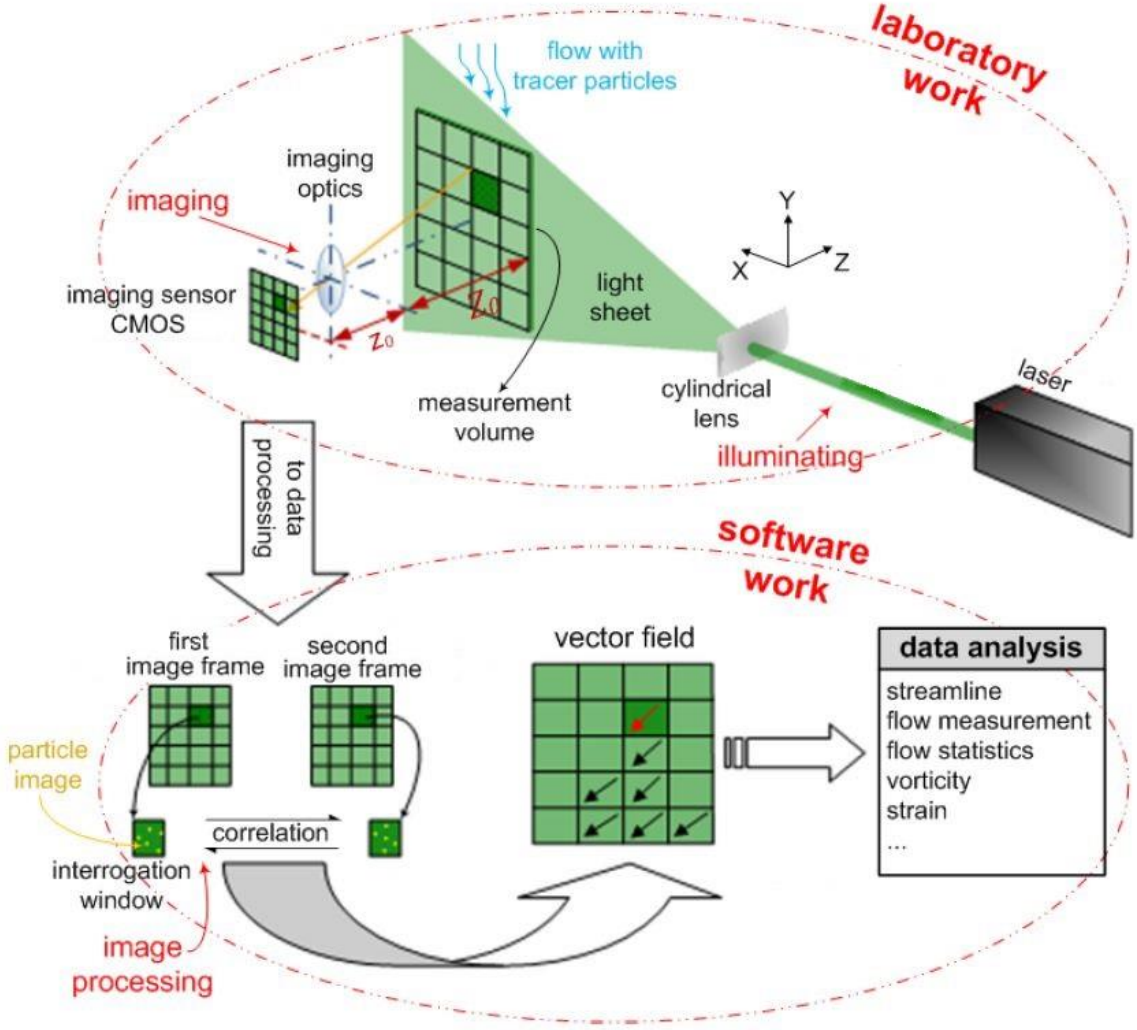

Figure 4.1: Common PIV procedures from data acquisition to data analysis. Figure modified from [25].

The general idea of PIV is based on adding tracer particles, also called seeding particles, to the fluid in motion. A laser with an optical arrangement such as a cylindrical lens forms a light sheet. When the fluid flow passes through the illuminated cross section of the flow duct, light will scatter from these seeding particles and recordings can be taken. The camera is usually located perpendicular to the light sheet. The displacement of the particles between the recorded images can then be determined by evaluating the PIV recordings in complex software by cross-correlating two images with a time delay between them. Velocity profiles, vortices and fluid displacement are few of many things one can extract from post-processing of PIV data. Regular practice is using a double-pulsed laser, which is synchronized with the camera, in such a way that images are acquired simultaneously as the laser is pulsed. However, in the work done for this thesis, the laser was continuously on for the duration of the image acquisition [26].

The PIV measures two variables, displacement and time increments, which is the fundamental definition of what we call velocity. Unlike other well-known methods of measuring velocity such as laser Doppler velocimetry, PIV gives entire fields of the velocity vector. In comparison with using methods of studying flow pattern by illuminating molecules or dye, PIV offer more robustness from using tracer particles as they scatter much more light. The seeding particles localize the velocity measurements, and will neither deform nor diffuse in time.

The rate of which the particles are moving is obtained by recording images of the particles at two defined times and deducting the displacement of the particles from the displacement of the images. The velocity can be estimated by the definition [27]:

$$U_p = \lim_{\Delta t \to 0} \left(\frac{\Delta s}{\Delta t} \right) \tag{4.1}$$

Where Δs and Δt denotes the displacement and time step respectively.

The most important idea behind PIV is the combination of quantitative and simultaneous measurements at several points in time. The ability to acquire several thousands of images in a split second makes PIV a rather easy and reliable method. Image recording can take place in the laboratory and later analyze offline and outside the flow facility.

Even though the idea and concept behind PIV seems intuitively simple on one hand, the factors that need to be taken into consideration in order to design and implement PIV experiments that delivers reliable, accurate, and fast measurement results are enormous. The work behind a proper PIV experiment include many scientific disciplines such as advanced optics, laser

operation, image and processing interpretation and processing and for not to mention, health and safety precautions. In this thesis, the PIV technique has been utilized to both qualitatively and quantitatively visualize flow fields concerning velocity profiles in the $\boldsymbol{u}$ direction [23]. Although the PIV method offers the ability to study and visualize the flow field without altering the flow behavior, some important factors need to be taken into consideration such as:

- Particle size
- Density difference between particles and fluid
- Velocity lag of particles
- Constant fluid acceleration

4.1 Seeding Particles

PIV is an indirectly method of measuring, as it is the particle velocity which is determined and not the fluid velocity. Therefore, the fluid's mechanical properties must to be known in order to avoid significant inconsistencies between the particles and fluid in motion. Among several other factors, the particle size is of great importance when conducting PIV experiments. Although the particle size depends on the scale that shall be resolved, the particles should be small enough to ensure good tracking of the fluid in motion, but large enough to ensure adequate light scattering. A compromise between these two should be made. In order to achieve a tracing accuracy below 1%, the particle Stokes number (response time) should be below 0.1. The stokes number is the ratio between the characteristic time of a particle and a characteristic time of the flow or an obstacle [28, 29]:

$$St = \frac{\tau_p u_f}{l_0} \tag{4.1}$$

Where,

$$\tau_p = d_p^2 \frac{\rho_p}{18\mu}$$

Here, τ_p represents the relaxation time of the particle, u_f is the velocity of the fluid and l_0 is the characteristic dimension of the obstacle, which is typically its diameter. Other symbols include d_p, ρ_p which is the diameter and density of the particle, respectively. The Greek symbol μ denotes the fluids dynamic viscosity.

The particles should have the same density of the fluid in order to prevent particle settling while performing experiments. The type of particles that are most often used in water and water solutions are polyamide seeding particles (PSP) in the order of 5-50 μm. Having a fluid with constant acceleration is desirable, if not the particle motion equation becomes more difficult to solve when post-processing the PIV recordings.

Figure 4.2: Polyamide seeding particles [30].

The polyamide seeding particles does not have an exact spherical shape as they are produced by a polymerization process. Other types of seeding particles do exist, such as hollow glass spheres (HGS), silver-coated hollow glass spheres (for increased reflectivity) and fluorescent polymer particles (FPP), which are all spherical but have somewhat higher density than PSP [30].

4.2 Light Source

Due to its high and stable light intensity, it is common to use an Nd: YAG laser (Neodymium Yttrium Aluminum Garnet) as a light source [31]. The one used in this thesis while performing the experiments is a DPGL-2200 L (Diode Pumped Green Laser) with the following specifications:

Table 4.1: DPGL-2200 L specifications.

Optical parameters	Specification
Wavelength	532 nm
Output Power	200 mW
Beam Diameter	1.0 mm

Figure 4.3: Illustration of the DPGL-2200 L Nd: YAG laser [32].

4.3 Image Acquisition

There are usually two choice of imaging sensors in digital PIV cameras today; Charged Coupled Device (CCD) or Complementary Metal Oxide Semiconductor (CMOS). Both having a technology that has evolved greatly the last years. CMOS is the type of imaging sensor in the camera used to acquire the images in this thesis and has the following specifications:

Table 4.2: Basler acA800-510um camera specifications [33].

Sensor	PYTHON 500
Shutter	Global shutter
Max. Image Circle	1/3.6”
Sensor Type	CMOS
Sensor Size	3.8 mm x 2.9 mm
Resolution (H x W)	800 px x 600 px
Resolution	CCIR
Pixel Size (H x W)	4.8 µm x 4.8 µm
Max. Frame Rate	511 fps
Mono/Color	Mono

The advantages with a CMOS image sensor is that pixels can be read out quickly from any region of interest making this digital sensor very suitable for time-resolved or dynamic PIV.

Another word for the CMOS sensor is the *active pixel sensor*, because it incorporates circuitry for each pixel that carries out signal processing such as pre-amplification and location readout. However, the CMOS sensors are typically less sensitive than the CCD image sensors. This implies that they require a larger sensor area, typically 20×20 μm^2, resulting in a larger bias error between the mean difference of the measured and actual particle displacement.

4.3.1 Particle Imaging

The main task of the camera and the lens is to obtain the location of the *p*th particle in the fluid, $\boldsymbol{x}_p(t)$, with respect to the location of its *image* on the camera, $\boldsymbol{X_p}(t)$.

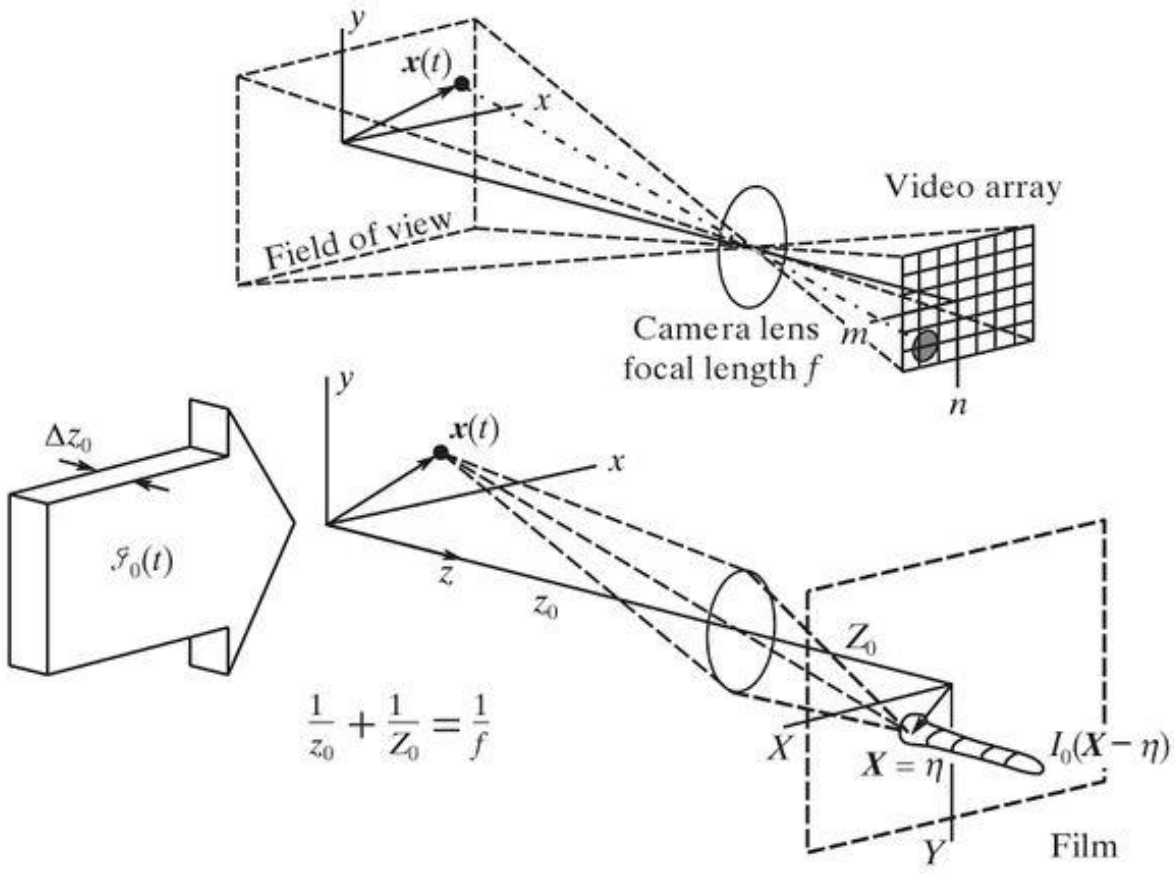

Figure 4.4: Single particles in the object plane are mapped to spots on plane surface of the camera [34].

The center of the image of a single particle in the light sheet, or $z = 0$ plane, is located by following a straight line from the object point through the effective center of the lens to the image plane, when using a lens with constant lateral magnification. The image containing the particle in the $(x, y, 0)$ plane is now mapped onto the (X, Y) image plane according to:

$$\begin{pmatrix} X \\ Y \end{pmatrix} = M_0 \begin{pmatrix} x \\ y \end{pmatrix} \tag{4.2}$$

Where the lateral magnification M_0 is equal to:

$$M_0 = \frac{Z_0}{z_0}$$

Here, x and y are the coordinates in the light sheet while X and Y are the coordinates on the image sensor. Z_0 is the image distance from the effective center of the lens to the image sensor and z_0 is the objective distance from the light sheet to the lens.

An object is in focus when all other light rays reflected from that object are refracted by the lens in such a way that they converge onto a point on the image plane. *Gauss lens law* describes at which conditions the points in the object plane (light sheet) are focused onto the image plane:

$$\frac{1}{Z_0} + \frac{1}{z_0} = \frac{1}{f} \tag{4.3}$$

Where f is the focal length.

An image is taken at time t and light scattered from the particles in the light sheet is captured on the camera image plane. A second image is taken at time $t + \Delta t$. By measuring the particle displacement $\Delta \boldsymbol{X}_p$ between the first and second image, we can find the particle's in-plane velocity components from equation (4.5). If we simultaneously assume that the time between capturing images is short enough to make the first-order time difference accurate and the imaging obeys equation (4.3), then:

$$\left(v_{px}, v_{py}\right) \cong \frac{\left(\Delta x_p, \Delta y_p\right)}{\Delta t} = \frac{\left(\Delta X_p, \Delta X_p\right)}{M_0 \Delta t} \tag{4.4}$$

Where the first expression represents the mapped particle velocity in x- and y-direction respectively.

The seeding particles will of course travel throughout the entire volume of flow, not just in the light sheet where, $z = 0$. All illuminated particles within this plane, focused or not will create images. The finite value of the diameter of the image can be approximated by combining the finite diameter of the particles, d_p along with the effect of lens diffraction and geometric aberration:

$$d_\tau = (M_0^2 d_p^2 + d_s^2 + d_a^2)^{\frac{1}{2}} \tag{4.5}$$

Where the diffraction diameter is defined by:

$$d_s = 2.44(1 + M_0) f^{\#} \lambda \tag{4.6}$$

And the lens aperture number is defined by:

$$f^{\#} = \frac{f}{D_a} \tag{4.7}$$

Here D_a is the diameter of the lens aperture, λ represents the light wavelength and d_a in equation (4.6) is the aberrated image diameter of a point source.

There are many reasons why optimization of the particle image diameter is necessary. The errors obtained in PIV velocity measurements are strongly dependent on the particle image diameter. The error can be mitigated by reducing the image diameter d_τ and the uncertainty of finding the center of the image plane or correlation peak respectively.

The depth of field in focus is given by:

$$\delta z \cong 4\left(1 + \frac{1}{M_0}\right)^2 f^{\#} \lambda \tag{4.8}$$

As the diameter of the particle image is dominated by diffraction, it is approximately independent of depth of field, which is represented by the z-axis. Approximately all particles, which are located within $\pm \delta z/2$ of the nominal object plane, will produce images that are in focus. In order to make sure that all particles in the light sheet are in focus, one can select proper values for $f^{\#}$ and M_0, so that $\delta z > \Delta z_0$. This can be done by decreasing the aperture to increase $f^{\#}$. This will decrease the amount of light that the image-sensing element is exposed to.

Table 4.3: Some theoretical values for diffraction limited imaging of small particles, where $\lambda = 532$ nm, $M = 1/4$ and $d_p = 1$ µm [35].

$f^{\#} = f/D_a$	$d_\tau\ [\mu m]$	δz [mm]
2.8	4.7	0.5
4.0	6.6	1.1
5.6	9.1	2.0
8.0	13.0	4.2
11	17.8	7.8
16	26.0	16.6
22	35.7	31.4

As it now has been presented that the depth of field is in fact finite, one cannot assume that the images captured by the camera are particles travelling in plane where $z = 0$. Therefore equation (4.3) must be adjusted to:

$$\begin{pmatrix} X_p \\ Y_p \end{pmatrix} = M_0(z_p) \begin{pmatrix} x_p \\ y_p \end{pmatrix} \tag{4.9}$$

Where the magnification of a particle at $z \neq 0$ is

$$M_0(z_p) = \frac{Z_0}{z_0 - z_p} \tag{4.10}$$

From equation (4.9), one can see that a particle, $\boldsymbol{x}_p$ in a three-dimensional space is mapped onto a two-dimensional image. Consequently, the particle image displacement will likewise depend on all three components of the particle displacement:

$$\begin{pmatrix} \Delta X_p \\ \Delta Y_p \end{pmatrix} = M_0 \begin{pmatrix} \Delta x_p \\ \Delta y_p \end{pmatrix} + M_0 \begin{pmatrix} x_p/z_0 \\ y_p/z_0 \end{pmatrix} \Delta z_p \tag{4.11}$$

Approximating this solution for a two-dimensional flow, where zero velocity exist in the z-direction ($\Delta z_p = 0$), so that $x_p \ll z_0$ and $y_p \ll z_0$, we achieve the following equation where the two-dimensional particle displacement can be found from the two-dimensional image displacement:

$$\begin{pmatrix}\Delta X_p\\ \Delta Y_p\end{pmatrix} \cong M_0 \begin{pmatrix}\Delta x_p\\ \Delta y_p\end{pmatrix} \tag{4.12}$$

Experiments utilizing planar PIV methods often achieve a combination of particles located both weakly out-of-plane and paraxial, which makes the equation above reasonably accurate [36].

4.4 Processing

After acquiring images from PIV experiments, both pre- and post-processing of the raw data are necessary to extract the desired information from the images.

4.4.1 Pre-Processing

Prior to performing vector computation, several manipulations can be done to the raw data in order to increase the quality of the results.

Contrast Limited Adaptive Histogram Equalization (CLAHE)

This pre-processing option enhances the contrast of the greyscale in the image, allowing to see particles which are partly out of plane.

High Pass Filter

The high pass filter passes signals with a frequency higher than a certain cutoff frequency and reduces signals with a frequency lower than the cutoff frequency. In simple terms, this enables the user to sharpen the image by means of removing background signal.

Intensity Capping

This option introduces an upper limit to the grayscale intensity of the image and reduces the influence of very bright particles.

Below are three images where the first presents the original unprocessed image. The second image is pre-processed with a high pass filter and the last with the CLAHE [37, 38, 39]

Original PIV image **High pass Filter** **CLAHE**

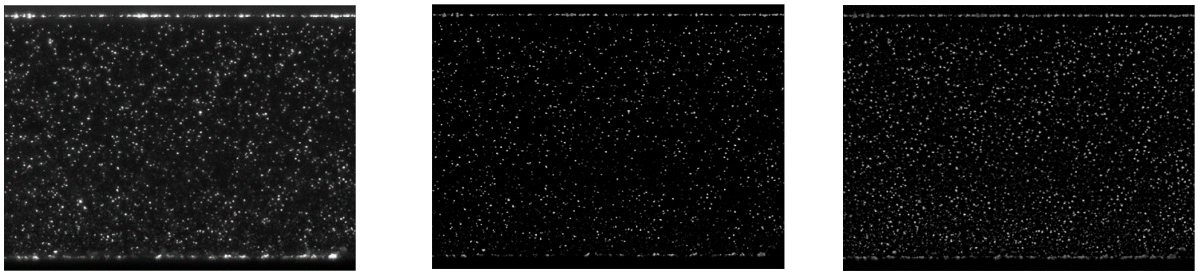

4.4.2 Post-Processing

As previously mentioned, one of the concepts of PIV is to create vector fields by measuring the traveled distance of the seeding particles. Processing images can be done in different ways. One is based upon auto-correlation analysis of multiple images captured on a single frame. However, the method used in this work, which is the most common way, is to capture several images on different frames and performing cross-correlation to measure the particle displacement. Cross-correlation measures the similarity of an image pair as a function of the relative displacement of the particles.

4.4.2.1 Cross-Correlation

Cross-correlation is the backbone of PIV and is in simple terms a technique to derive the most probable particle displacement in the interrogation areas by matching particle patterns from interrogation area 1 with interrogation area 2. The local displacement vector for imaged tracer particles of the first and second image is determined for each interrogation area by means of statistical methods, considering the time delay between the two images, the size and intensity of each pixel on the image and the magnification of the imaging. The use of temporal and spatial resolution to conduct detailed analysis of the physical properties of a flow are one of many advantages to why PIV often is applied to compare experimental and numerical results.

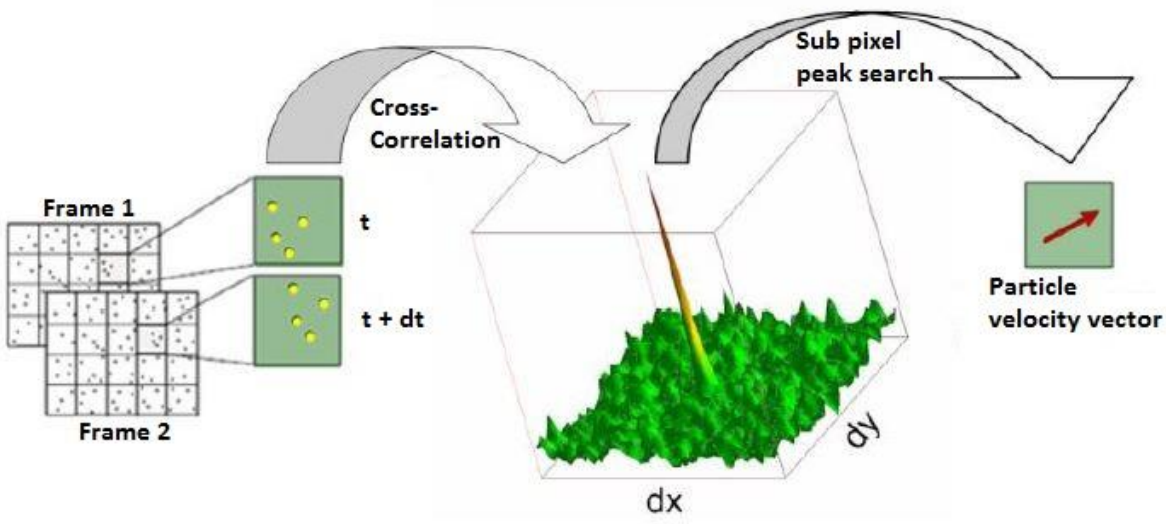

Figure 4.5: Cross-correlation of two frames to yield a velocity vector. Modified figure from [40].

Considering two images with the intensities I_1 and I_2, where each image consists of $X \times Y$ pixels divided into interrogation areas of $M \times N$ pixels. The cross-correlation $R_{I_1 I_2}(m,n)$ is equal to

$$R_{I_1 I_2}(m,n) = \frac{1}{N^2} \sum_{i=0}^{M-1} \sum_{j=0}^{N-1} I_1(i,j) I_2(i+m, j+m) \tag{4.13}$$

The correlation peak represents the displacement for each interrogation window. An alternative to cross-correlating directly in the spatial domain, one can apply the correlation theorem, which states that the cross-correlation of two functions is equivalent to a complex conjugate multiplication of their Fourier transforms:

$$R_{I_1 I_2} \Leftrightarrow \hat{I}_1 \cdot \hat{I}_2^*$$

Where $\hat{I}_i$ is the Fourier transform of I_i and * denotes complex conjugate. This can now be implemented using Fast Fourier Transform (FFT) algorithm, which is by far faster than cross correlating in the spatial domain. FFT is probably the most commonly used method of calculating displacement in PIV post-processing.

Since the input in the FFT algorithm is assumed to behave periodic, the correlation data is also periodic. Any real displacement larger than half of the interrogation area will then be replaced by its alias, resulting in displacements $d_{x,true} > M/2$ will be replaced by the alias, $d_{x,measured} = d_{x,true} - M$.

Information about the signal to noise ratio can be found by comparing the highest peak in the correlation plane with the remaining peaks in the plane. It is therefore valuable to evaluate the degree of correlation between two different interrogation areas. If the two compared interrogation areas have different particle intensities, the standard cross-correlation equation (4.14) will result in different peak heights for the same degree of matching. Therefore, it is widely common to take use of normalized cross-correlation with background subtraction (as stated in [41])

$$C_{I_1 I_2}(m,n) = \frac{1}{N^2} \frac{\sum_i \sum_j [I_1(i,j) - \mu(I_1)][I_2(i+m, j+n) - \mu(I_2)]}{\sum_i \sum_j \sqrt{[I_1(i,j) - \mu(I_1)]^2 [I_2(i+m, j+n) - \mu(I_2)]^2}} \tag{4.14}$$

Where $\mu(I_i)$ denotes the mean of imageI_i. It is now possible to directly compare the degree of matching in the two different interrogation areas, by using this normalization. However, the

term in the denominator is complicated to implement in a FFT scheme. Equation (4.15) is then usually approximated to:

$$C_{I_1 I_2}(m,n) = \frac{1}{N^2} \frac{\sum_i \sum_j [I_1(i,j) - \mu(I_1)][I_2(i+m, j+n) - \mu(I_2)]}{\sigma_{I_1} \cdot \sigma_{I_2}} \tag{4.15}$$

Where σ_{I_i} symbolizes the standard deviation of image I_i [42].

4.4.2.2 Multiple Pass Interrogation

As opposed to the previously discussed displacement estimation, multiple pass repeatedly interrogates the same PIV image pair using the same dimensions of the interrogation domain. The multiple pass approach use the first pass as a predictor for the displacement to shift the location of the interrogation windows, such that the window offset is refined for the subsequent interrogation passes. The multiple pass technique is often used together with a subpixel window shift or window deformation algorithm. The end goal is to enhance the number of particle image pairs in the common interrogation domain. This results in reduced bias, loss of correlation and random estimation errors, which ties back to increased accuracy and signal to noise ratio. By symmetrically shifting the image pair, the displacement will correspond to a central difference interrogation (CDI) [43]. As opposed to forward difference interrogation (FDI), the CDI scheme which is second order accurate in time, delivers results that are more accurate and can maximize the signal to noise ratio. The FDI scheme calculates the velocity at time t by utilizing images recorded at times t and Δt. The Taylor expansion of $x(t + \Delta t)$ will then be:

$$x(t + \Delta t) = x(t) + \Delta t \frac{dx}{dt}(t) + \frac{(\Delta t)^2}{2!} \frac{d^2x}{dt^2}(t) + \cdots \tag{4.16}$$

If we reorganize the equation above and define the velocity as $V(t) = \frac{dx}{dt}(t)$, we arrive at:

$$V(t) = \frac{x(t + \Delta t) - x(t)}{\Delta t} + o(\Delta t) \tag{4.17}$$

The CDI scheme approximates the velocity at time t by symmetrically shifting the two images. The Taylor expansion of $x(t + \Delta t/2)$ will then be:

$$x\left(t + \frac{\Delta t}{2}\right) = x(t) + \frac{\Delta t}{2}\frac{dx}{dt}(t) + \frac{\left(\frac{\Delta t}{2}\right)^2}{2!}\frac{d^2x}{dt^2}(t) + \frac{\left(\frac{\Delta t}{2}\right)^3}{3!}\frac{d^3x}{dt^3}(t) + \cdots, \tag{4.18}$$

and likewise, for $x(t - \Delta t/2)$

$$x\left(t - \frac{\Delta t}{2}\right) = x(t) - \frac{\Delta t}{2}\frac{dx}{dt}(t) + \frac{\left(\frac{\Delta t}{2}\right)^2}{2!}\frac{d^2x}{dt^2}(t) - \frac{\left(\frac{\Delta t}{2}\right)^3}{3!}\frac{d^3x}{dt^3}(t) + \cdots. \tag{4.19}$$

By adding equation (4.19) and (4.20) we achieve the following result:

$$V(t) = \frac{x\left(t + \frac{\Delta t}{2}\right) - x\left(t - \frac{\Delta t}{2}\right)}{\Delta t} + o((\Delta t)^2) \tag{4.20}$$

and therefore, showing that the CDI scheme is in fact second order accurate in time [42].

4.4.2.3 Multiple Grid Interrogation

Multiple grid interrogation, which is often shortened down to multigrid interrogation, is similar to multiple pass interrogation. However, while the dimension of the interrogation area remains the same for multiple pass interrogation for each step, it is reduced for each subsequent pass for multiple grid interrogation and the interrogation grid is refined. The first pass can for example be a rather large interrogation domain and corresponding grid of 128 × 128 pixels. The results from the first pass are interpolated to match a smaller interrogation domain with corresponding grid of typically 64 × 64 pixels. This is then used for the subsequent interrogation passes. The process is repeated until the desired resolution is reached.

Compared to multiple pass interrogation, the multiple grid approach assures that the in-plane loss of correlation remains small by reducing the interrogation domain for each subsequent pass. However it is common to combine both the approaches of multiple grid and multiple pass (with subpixel estimation and window deformation interrogation) once the desired interrogation resolution has been achieved.

4.4.2.4 Window Deformation

The standard image-processing algorithm using cross-correlation through FFT provides somewhat of acceptable velocity vector. However, by interrogating windows which are fixed in size and position, its accuracy becomes deteriorated and sometimes yield erroneous vectors due to loss of particles data acquisition region. In order to compensate for these losses of pairs, the window in the second image should be deformed according to the displacement information resulting from the first image. This is carried out by interpolation. Several interpolation methods are used, such as bilinear interpolation which is fast, or spline interpolation which delivers higher precision at the cost of computational time.

The figure below presents the principle of window deformation. The first interrogation pass will yield nine positions within the interrogation area, showing the displacement information. This information is interpolated by one of the approaches discussed above to derive the displacement of each pixel in the interrogation area. Finally, the window in the second image is deformed, followed by several interrogation passes [37, 44].

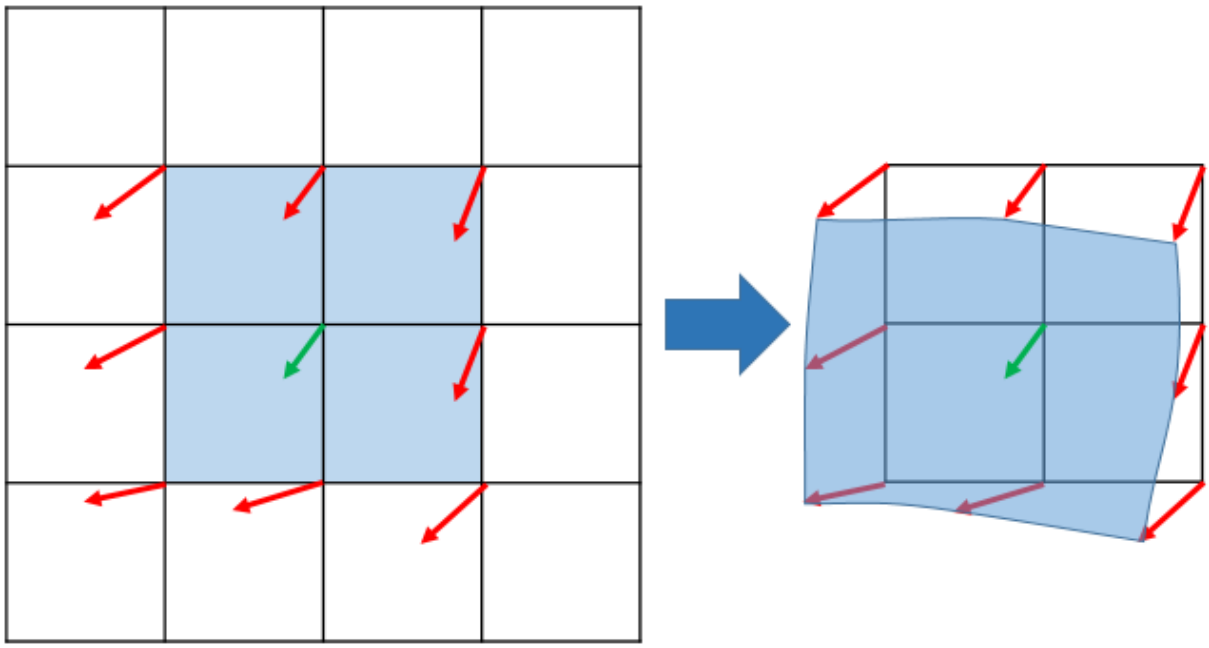

Figure 4.6: Principles of window deformation.

4.4.2.5 Sub Pixel Displacement Estimation

This technique improves the displacement estimation accuracy by taking use of sub pixel estimation of the correlation peaks. The common procedure is to fit a Gaussian function to the peak and the adjacent vertical and horizontal points in the correlation plane. Normally a two

times three point fit is used. The peak fitting function also introduces a bias called peak locking, as they usually tend to lock in on integer of pixel locations. The implementation of a continuous window shift by interpolating the images at intermediate locations between pixels will help reduce the peak locking effect. The interrogation windows are shifted dynamically until the sub pixel displacement estimation reaches zero [42, 45]

Some of the vast mathematical and physical background of imaging, pre- and post-processing techniques has been discussed in this chapter. However, this is only a fraction of what lies behind this method of both qualitatively and quantitatively visualizing a fluid in motion. For further detailed material, the reader is referred to [46, 47].

5 Experimental Design

In this chapter there will be presented several procedures done to finalize the design of the flow duct and the accompanying fluid, including practical, as well as extensive analytical work. The experiments conducted in this thesis are based on a field size mud conditioning operation performed between a $9^{5/8}$-in. casing and a $12^{1/4}$-in. borehole. Regular parameters while conditioning such an annulus are presented in the table below.

Table 5.1: Field conditioning values.

Parameter	Value	Unit
Flowrate, q	1400-2100	lpm
PV	20,0	cp
PV	0,02	Pa.s
YP	12,0	lbs/100 ft^2
YP	5,75	Pa

With regards to the table above, the yield point has been converted to Pa by multiplying the given value in lbs/100 ft^2 by a factor of 0, 4788.

Scaling these parameters down to suitable field values were done by maintaining similar Bingham numbers for the field and laboratory case, which results in a velocity profile matching. Two scaling methods were done. Firstly, the circular geometry of the field case needed to be represented as a slot configuration at a convenient laboratory size. Secondly, the rheological parameters were scaled down to laboratory conditions. These scaling methodologies are presented in the subsequent chapters.

5.1 Flow Channel Design

In the following chapter, the slot configuration method of the field annulus is presented before it is scaled down to a convenient laboratory size. Subsequently, literature and studies were investigated to verify the correct aspect ratio for the flow channel.

5.1.1 Slot Representation of the Annulus

Flow of fluid through an annular section can also be represented as flow through a rectangular slot by utilizing equations developed for this purpose. The slot flow equations are somewhat easier to use and are fairly accurate as long as the ratio between the inner and outer diameter of the pipe is less than 0,3 [48].

Representing the annulus as a rectangular slot was done for PIV purposes. Conducting PIV experiments through an annular representation of the field case was intuitively thought of to yield problems concerning the laser and image acquisition. Having the laser sheet configured to go through a two-pipe cylindrical experimental equipment would result in undesirable light reflections. Capturing images through a curved surface would also not be optimal and difficult. By representing the annulus as a rectangular slot, experimental procedures were simplified.

The figure below illustrates the annulus as a slot representation.

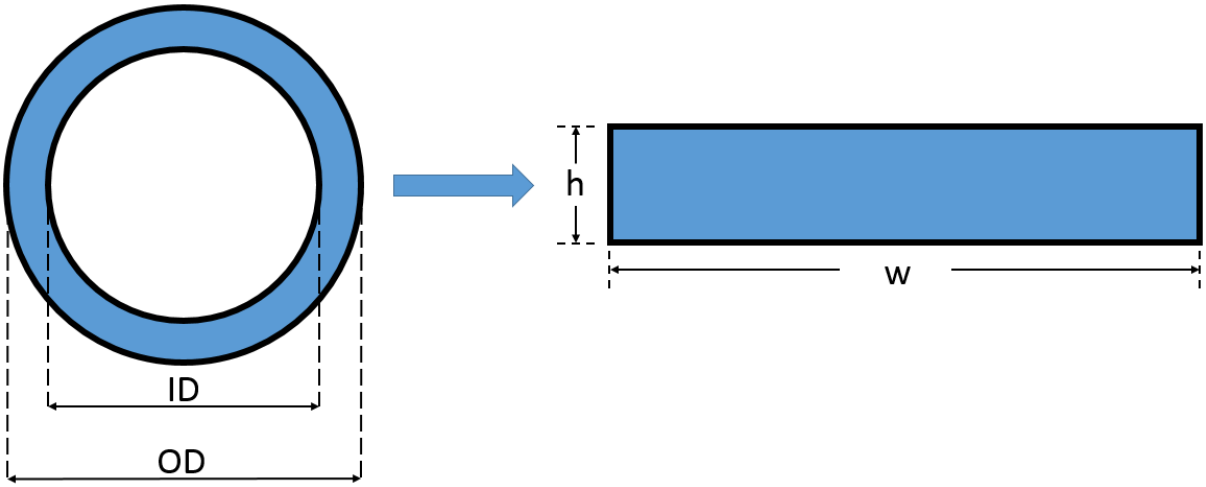

Figure 5.1: Slot configuration of an annulus.

The height and width of the rectangular slot can be calculated by the following equations:

$$w = \pi \frac{OD + ID}{2} \tag{5.1}$$

$$h = \frac{OD - ID}{2} \tag{5.2}$$

The next task at hand is to find which height and width that was desirable for the flow duct to be designed. A look at the slot configuration of the field casing and annulus is a good starting point, which is presented in the table 5.2.

Table 5.2: Slot conversion of annulus dimensions.

Parameter	Unit	Value
Annulus	cm	12,25
Casing	cm	9,625
Slot Height, h	cm	3,33
Slot Width, w	cm	87,3

As seen in table 5.2, a height of 3,33 centimeters would be manageable, but a width of 87,3 centimeters would be too large for an experimental flow duct to fit into the laboratory station at hand. A width of almost one meter would also result in large amount of fluids to be mixed up for each run, which is time consuming and neither suitable nor economical. It was decided that a height half of this, rounded up to 1,7 centimeters would be sufficient with regards to the PIV measurements. Now that the height of the flow channel was established, the next task at hand was to find the aspect ratio needed in order for the wall effects to be negligible for a finite wide duct when measuring in the middle of the flow channel. The analytical work behind that is mentioned in the next subchapter.

5.1.2 Flow Channel Aspect Ratio

In order to neglect the side wall effects for a Newtonian fluid in the flow channel, the sufficient aspect ratio needed to be determined. Holmes and Vermeulen (H&V) (1968) studied *velocity profiles in ducts with rectangular cross section* and presents the following equation in the article with the same name [49].

$$v \Big/ v_{max} = V = \frac{\sum_{k=1,3,5..}^{\infty} (-1)^{1/2(k-1)} k^{-3} \cos\left(\frac{1}{2} k\pi\zeta\right) \left\{1 - \frac{\cosh\left(\frac{1}{2} k\pi\xi\, B/H\right)}{\cosh\left(\frac{1}{2} k\pi\, B/H\right)}\right\}}{\sum_{k=1,3,5..}^{\infty} (-1)^{1/2(k-1)} k^{-3} \left\{1 - 1/\cosh\left(\frac{1}{2} k\pi\, B/H\right)\right\}} \quad (5.3)$$

This equation presents the dimensionless velocity profile for a finite wide duct. As seen, it also contains the width and height of the duct which is denoted B and H, respectively. This equation can be compared with Poiseuille's equation (3.24) in chapter 3.7.2 to find an acceptable aspect ratio.

Firstly, Poiseuille's equation needs to be presented in its dimensionless form, like equation (5.3), in order to be comparable. We first recall the definition of $u(y)$ and u_{max}:

Defined from equation (3.24):

$$u(y) = \frac{1}{2\mu}\left(\frac{\partial p}{\partial x}\right)(hy - y^2)$$

It has been shown that u_{max} is defined at $y = h/2$, which yields

$$u_{max} = \frac{h^2}{8\mu}\left(\frac{\partial p}{\partial x}\right) \tag{5.4}$$

Dividing $u(y)$ by u_{max} results in the dimensionless velocity profile:

$$\frac{u(y)}{u_{max}} = U = \frac{4}{h^2}(hy - y^2) \tag{5.5}$$

Secondly, as equation (5.3) is defined in a different coordinate system than equation (5.5), we need do redefine the coordinate system for the latter equation in order to compare. The coordinate systems are defined as seen in the figure below:

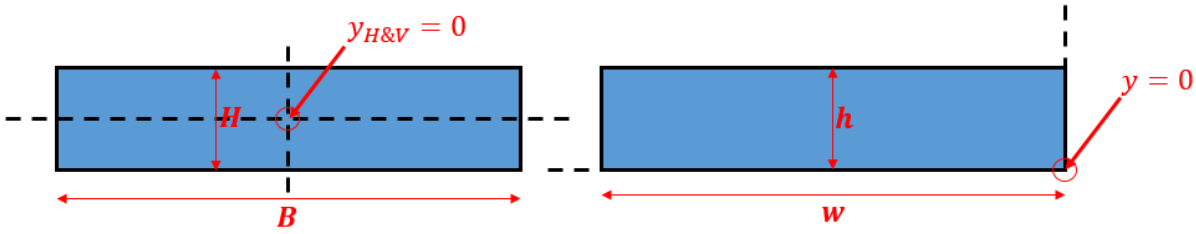

Figure 5.2: Slot coordinate systems.

The figure to the left represents the coordinate system in equation (5.3) and the figure to the right represents the coordinate system in equation (5.5)

We define the following relation for the coordinate system:

$$y = y_{trasnf} + \frac{h}{2}$$

Inserting this for y in equation (5.5) will represent the equation in the same coordinate system as equation (5.3)

$$U = \frac{4}{h^2}\left[h\left(y_{transf} + \frac{h}{2}\right) - \left(y_{transf} + \frac{h}{2}\right)^2\right]$$

Solving this for U will yield:

$$U = \left(1 - \frac{4{y_{transf}}^2}{h^2}\right) \tag{5.6}$$

An important note to recall is that equation (3.24) is derived for an infinite wide duct. Now that both equations are defined in the same coordinate system and made dimensionless, a comparison can be presented for given y-values. Note that $h = H = 1{,}7$ centimeters for both equations. A value of $B = 17$ centimeters were chosen for the comparison, giving an aspect ratio of 1:10.

Table 5.3: Comparison of Eqs. (5.6) and (5.3) for the same coordinate system.

Y [cm]	V	U
0	0	0
0,17	0,3600	0,3600
0,34	0,6400	0,6400
0,51	0,8400	0,8400
0,68	0,9600	0,9600
0,85	1	1

As showed in the table above, the equation (5.3) generates the same results as equation (5.6) for four significant decimal places, making an aspect ratio of 1:10 acceptable for the flow channel design.

Additional literature was studied to investigate if an aspect ratio of 1:10 would be sufficient. The work of Chakraborty (2008) presents the following equation [50]:

$$u(y,z) = -\frac{16a^2}{\pi^3}\left(\frac{1}{\mu}\frac{dp}{dx}\right)\sum_{n=0}^{\infty}\frac{1}{(2n+1)^3}\times$$
$$(-1)^n\left[1 - \frac{cosh\left(\frac{2n+1}{2a}\right)\pi z}{cosh\left(\frac{2n+1}{2a}\right)\pi b}\right]cos\left(\frac{2n+1}{2a}\right)\pi y \tag{5.7}$$

Where $2a$ and $2b$ denotes the dimension along the y- and z-axes, respectively. The coordinate system used here is similar as for the work of Holmes and Vermeulen (1968), placing the origin at the center of the cross section of the flow channel. However, it would be beneficial to present a figure of the coordinate system for the sake of clarity.

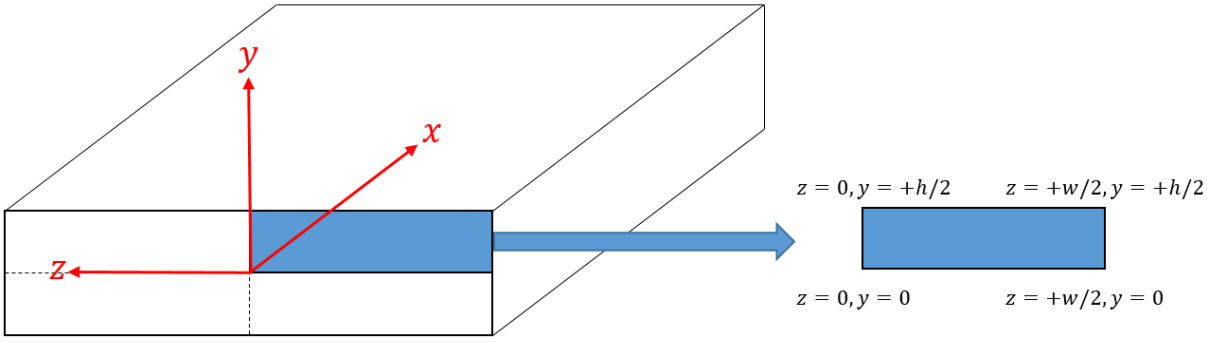

Figure 5.3: Representation of the Chakraborty [50] coordinate system.

Where the x- y- and z-axes represent the length, height and width of the channel, respectively. For reasons of simplicity, the total height and width of the channel is referred to as h and w.

The comparison between (5.7) and the predefined equation (3.24) for an infinite wide duct is solved in MATLAB. The result is shown in the figure below:

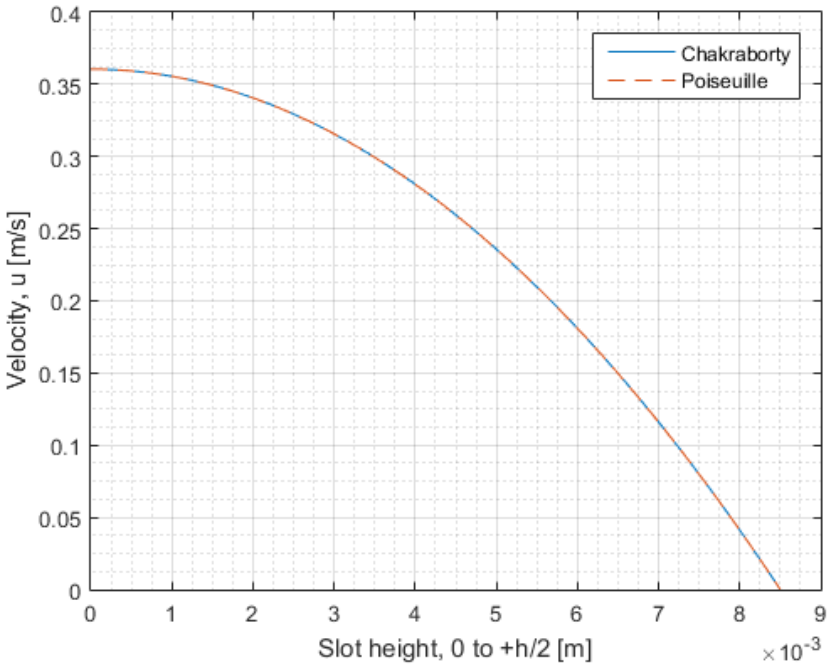

Figure 5.4: Comparison of Chakraborty and Poiseuille velocity equation.

Both equations have been solved for the plane $z = 0, y = +h/2$, which corresponds to the exact middle point of the flow channel. An aspect ratio of 1:10 has also been considered here.

Equation (3.24) in the MATLAB code is referred to as Poiseuille's equation with the same coordinate system shift as in Holmes and Vermeulen. To clarify this, an explanation is shown here, where $u(y)$ is expressed by the dimensionless U and u_{max}.

$$u(y_{transf}) = U \times u_{max} = \frac{h^2}{8\mu}\left(\frac{\partial p}{\partial x}\right)\left(1 - \frac{4{y_{transf}}^2}{h^2}\right) \tag{5.8}$$

One additional aspect ratio validation was conducted. This time for a Bingham plastic fluid. For a Newtonian fluid, the Navier-Stokes equations become a Poisson equation, or equivalently a non-homogeneous Laplace equation, which can be solved as an infinite Fourier series. However, for a non-Newtonian case, the Navier-Stokes equations become a non-linear Poisson equation.

A code in C# had been designed to seek the solution of the two-dimensional Navier-Stokes equations for a Bingham plastic fluid in a finite wide slot. The well-known Newtonian velocity field was used as the initial trial guess, where the velocity field is iterative updated using the Gauss-Seidel method. The known velocity field is also used to evaluate the rate of strain tensor and the viscosity function [1].

Based on this, together with the work of Holmes and Vermeulen (1968) and Chakraborty (2008), an aspect ratio of 1:10 or lower was found theoretically to be acceptable for the flow channel design both for Newtonian and Bingham plastic fluids [49, 50]

5.1.3 Physical Design of the Flow Channel

In order to obtain a visual perspective of how the final flow channel would be designed, a smaller prototype was first built. As it was thought of giving the most optimal optical properties, glass was chosen as the material for the prototype. The thickness of the glass had to be thick enough to withstand cracking or bursting, and also be thin enough to mitigate refraction from light when conducting PIV experiments, although no PIV experiments were meant for the prototype. The purpose of the prototype was to give a general idea of how the final flow channel would be designed and in which material.

Both side walls and top and bottom walls consisted of 4 millimeters thick glass. The prototype was 20 centimeters long and fitted with aluminum plates at both open ends in order to screw in a ½ inch nipple to fit the fluid hose.

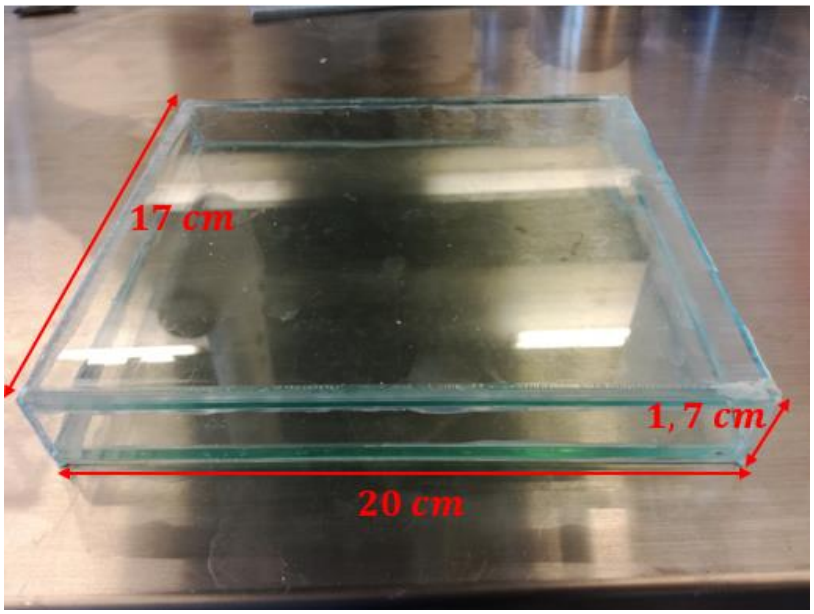

Figure 5.5: Prototype glass channel.

The dimension given in the figure above are the inside dimensions, except for 20 centimeters, which is the length of the glass channel.

The prototype was flooded several times with preliminary fluids to check if it could withstand the system pressure. Several leakages occurred during this period and repair jobs were carried out often. There were only one outlet and inlet in the prototype resulting in a jet stream of fluid in the middle of the channel and continuous vortices and eddies at both sides. A pure laminar flow in this short of a channel with clear streamlines was not achieved. Several different configurations were carried out with the prototype. For instance, a small fluid reservoir at both in and outlet to mitigate the turbulence in the fluid exiting the hoses were installed without resulting in any major success.

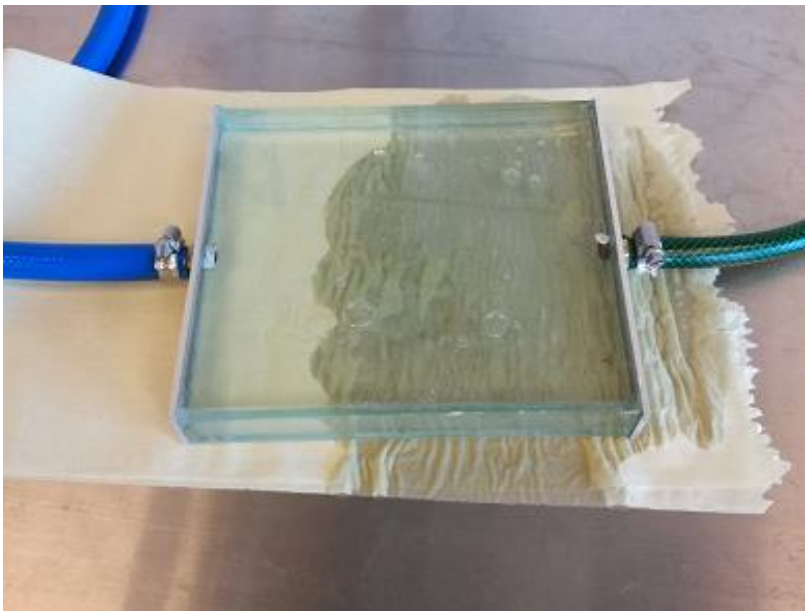

Figure 5.6: Leakage in prototype flooded with water.

A conclusion to this was that in the final design, the channel needed to be extended in length in order to account for entry effects and it would be desirable to have several inlets and outlets.

It was decided that the glass channel was to be flanged between two extension channels made of transparent acrylic and the PIV measurements were to be conducted at the glass channel. Two lengths of 85 centimeter acrylic channels were procured with the same internal dimensions as the glass channels. Each piece of the acrylic channels is attached together using a glue called Acryfix. The thickness of the top and bottom plate in the acrylic ducts are 6 millimeters, while the side plates measures 4 millimeters. The acrylic channels include an internal acrylic wall at start and end containing 16 x 3 millimeter diameter holes used to distribute the flow evenly. A figure of the channel layout is included below.

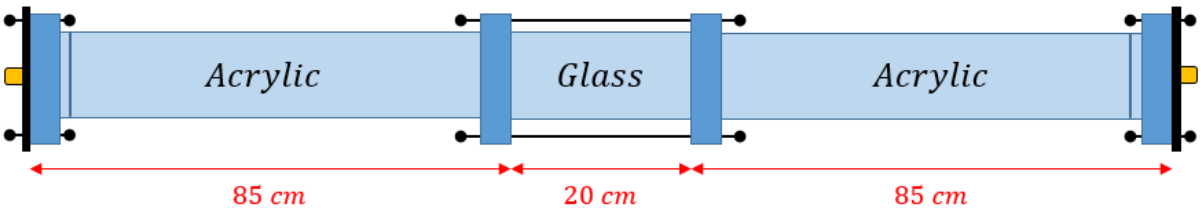

Figure 5.7: Illustration of the glass prototype flanged in between two acrylic channels.

The four dark blue regions represents the flanges used to connect end plates and flanging the glass channel between the acrylic ducts. The dark lines right after the first and right before the last flange illustrates the perforated internal wall. The black lines with knobs at each end represents the screws used to connect each end plate to the duct and the screws used to tighten

in the glass channel between the acrylic ducts. The orange nobs at each end of the figure represents the ¾ inch nipples that are screwed into the end plates where hoses can be connected.

The idea behind this setup seemed prominent, but flanging in the glass channel resulted in cracking the glass because of the compressional forces. The cracks in the glass channel is shown in the pictures below.

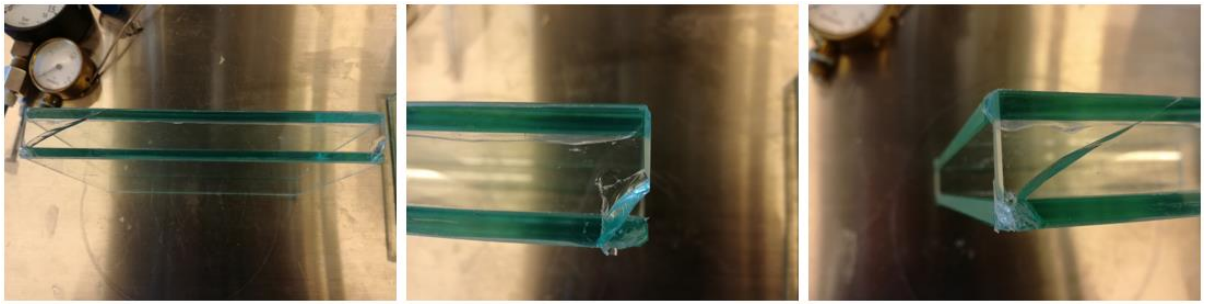

Figure 5.8: Prototype glass channel cracked at corners.

Having a glass channel flanged in between the acrylic flow channels was discarded. Continuing with a flow channel consisting of only acrylic was concluded to be sufficient with regards to optical properties. The two remaining acrylic channels of 85 centimeters each were instead flanged together as a starting point for preliminary PIV experiments.

The aluminum end plates at the start and end of the flow channel appeared to have insufficient strength when connecting it. The plates would buckle when screwing it to the channel. A substitute to the aluminum plates were two 1 centimeter thick steel plates in order to ensure no buckling when attaching them to the acrylic channels.

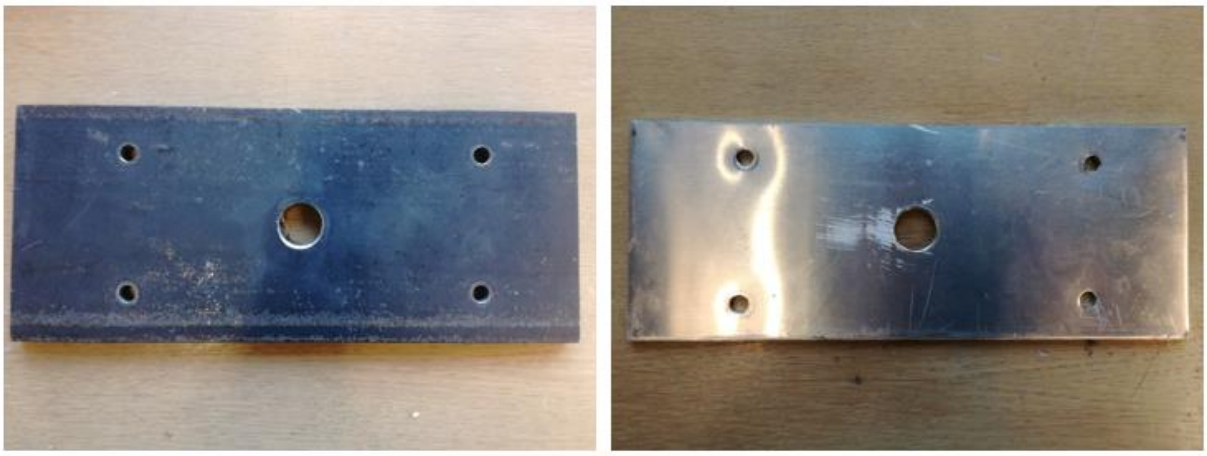

Figure 5.9: 1 centimeter thick steel end plate (right) and 3 millimeter thin aluminum end plate (left).

Designing a rectangular flow and pressure chamber is not desirable with regards to even pressure distribution along the surfaces, but for the experiments and purpose of this thesis it was necessary due to the slot configuration. During initial flow testing of the flanged acrylic flow channels, one channel cracked. The pressure inside the duct was not recorded at the time of failure. Whether it first failed in the glue or in the acrylic itself is unknown. A probable reason for the failure is stress concentration at the square corners. One may speculate that crack initiation started at the side wall due to reduced thickness compared to top and bottom wall. The picture below shows the cracked region of the duct.

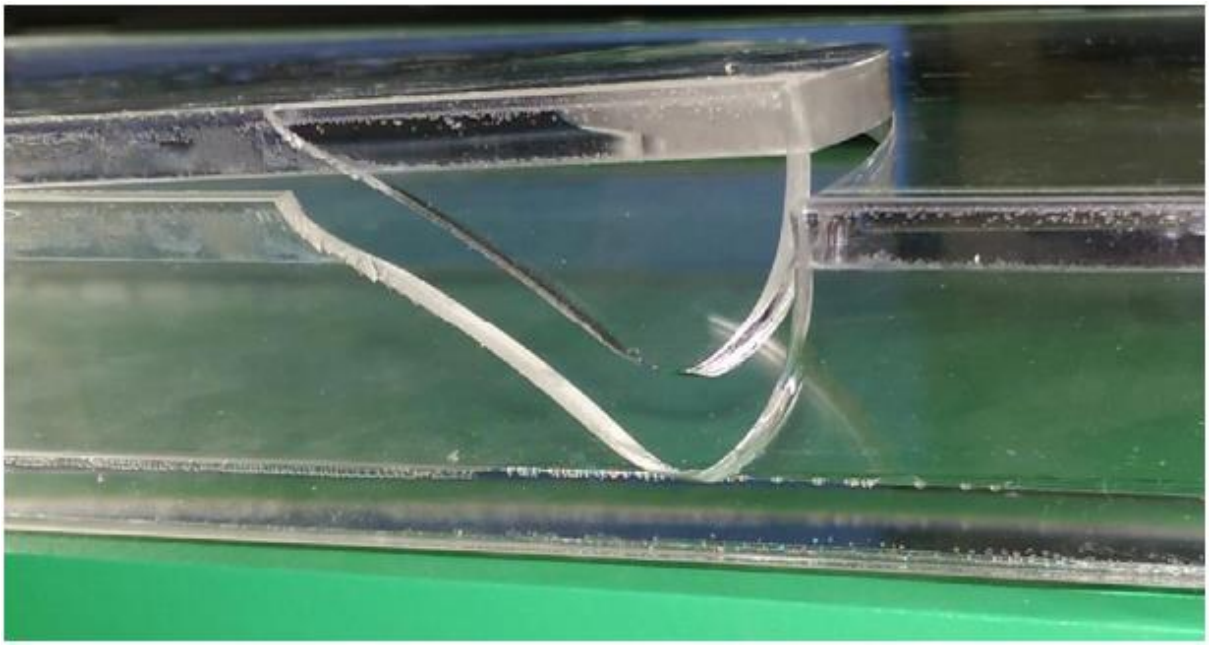

Figure 5.10: First crack in acrylic duct.

Next is a crack depicted that is located 60 centimeters away from the crack shown above. Both cracks are connected by the loosened top plate which is seen in the picture above.

Figure 5.11: Second crack in acrylic duct.

A solution to mitigate the pressure inside the channel and also to even out the flow going in and out of the duct was to reconfigure the start and end steel plates. Two new holes were drilled out, resulting in three holes in each steel plate. Two new holes were added to the end plate prior to adding it to the start plate. Figure 5.12 shows the system configuration having one hole in the start plate and three holes in the end plate.

The acrylic flow channel that did not crack was still usable and was reinforced with silicone at each corners of the channel to prevent potential future leakages.

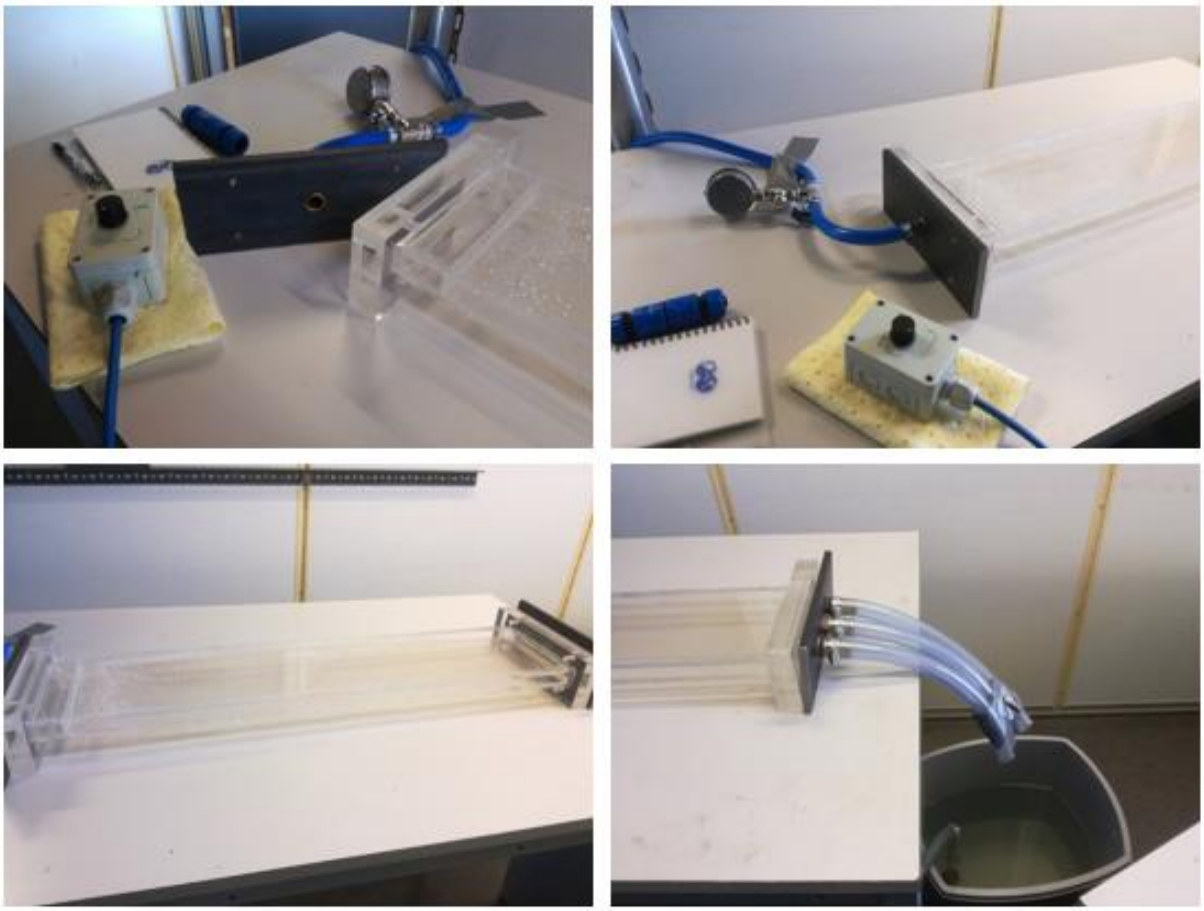

Figure 5.12: Early system layout.

A new and improved acrylic channel was procured, configured with three reinforcements placed evenly along the duct. This was chosen to prevent future cracking. The new channel was constructed with a different capillary glue which would penetrate the void spaces between the acrylic. The channel was then left overnight in an oven to relieve any residual stress in the acrylic applied under manufacturing.

Figure 5.13: New and improved acrylic channel.

The two remaining channels were flanged together, which were later used for the final PIV experiments conducted for the slot configuration of the regular geometry. As the start plate now was configured with three holes, a manifold system was necessary to connect the hose coming out of the pump to the three ¾ inch nipples screwed into the plate. By adding three holes on the start and end plate, the pressure mitigation was more than sufficient. The pressure gauge implemented in the flow loop showed now no more than 0,2 bara pressure.

Figure 5.14: Final flow channel setup used for PIV experiments.

The picture above shows the manifold system with three inlets and the flow channels both attached and detached with a cork gasket in-between for sealing. This is the final setup that was utilized for the PIV experiments. The flow would go from left to right considering the top picture. A simple schematic of the whole setup is shown in the figure below. The simple flowmeter used was a Gardena type to give a rough estimation of the flow rate. An analog pressure gauge was placed before entry of the duct to monitor the pressure in the channels.

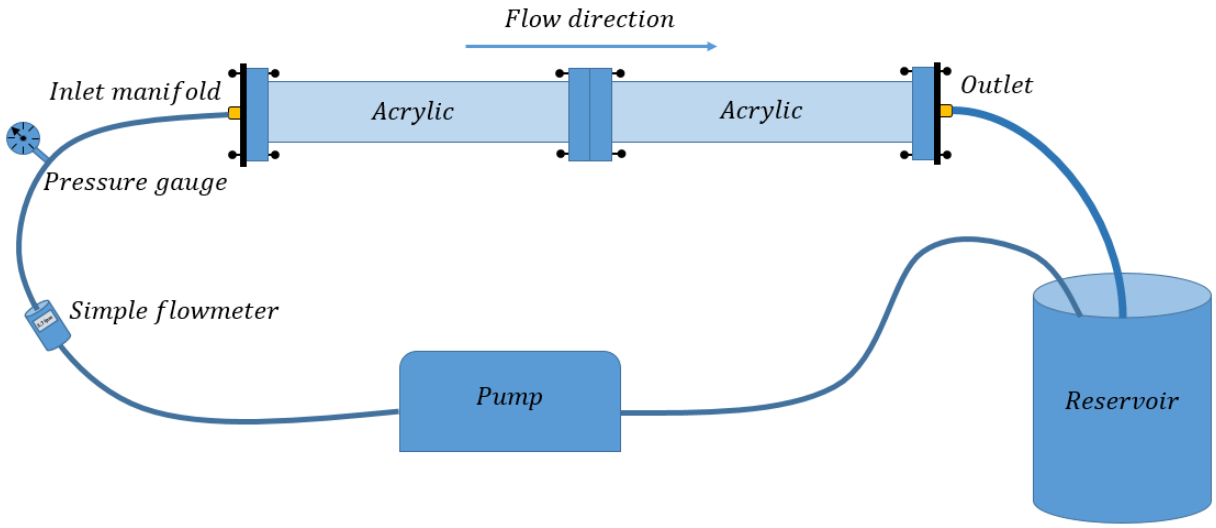

Figure 5.15: Schematic of the final flow channel setup.

5.2 Fluid Design

This chapter presents the time-consuming work behind the search for the laboratory equivalent Bingham plastic fluid. By matching the Bingham number for the field and laboratory case, fluid would yield the same velocity profile. Two cases of PIV experiments were conducted, a Newtonian fluid used as a reference and a Non-Newtonian fluid. The Newtonian fluid used was water and the Non-Newtonian fluid is described in chapter 5.2.2. First the scaling methodology is presented followed be the comprehensive rheological testing of several potential fluids.

5.2.1 Rheological Scaling

The rheological scaling method in this thesis is based on the simplification of the generalized Reynold's number [51]. From this simplification, we reach the result of the following relationship, which forms the start point of the scaling method:

$$\frac{Re_{GenBingham}}{He_{\mu=\mu_p}} = \frac{q_D^2}{1+8q_D} \tag{5.9}$$

The main important condition is ensuring that the relation between the Reynold's and Hedstrøm number to be kept constant when converting from field to laboratory case. This relation is also known as the Bingham number. In the analysis below, subscript A denotes the field case and subscript B denotes the laboratory case.

To maintain constant relation between Reynold's and Hedstrøm number:

$$\frac{q_{DA}^2}{8q_{DA}+1} = \frac{q_{DB}^2}{8q_{DB}+1} \tag{5.10}$$

$$(8q_{DA}+1)q_{DB}^2 - 8q_{DA}^2 q_{DB} - q_{DA}^2 = 0$$

$$q_{DB} = \frac{8q_{DA}^2 \pm \sqrt{64q_{DA}^4 + 4(8q_{DA}+1)q_{DA}^2}}{2(8q_{DA}+1)}$$

Simplifying the equation

$$q_{DB} = \frac{4q_{DA}^2 \pm (4q_{DA}^2 + q_{DA})}{(8q_{DA}+1)}$$

The minus sign is neglected as q_{DB} is greater than 1.

$$q_{DB} = \frac{8q_{DA}^2 + q_{DA}}{8q_{DA}+1}$$

Which results in:

$$q_{DB} = q_{DA} \tag{5.11}$$

Finally it can be concluded that:

$$\left(\frac{\mu_p \overline{u}}{\tau_y}\right)_B = \frac{h_B}{h_A}\left(\frac{\mu_p \overline{u}}{\tau_y}\right)_A \tag{5.12}$$

This equation has been solved for $\bar{u}_B$ in order to find the resulting flowrate for the laboratory conditions, yielding:

$$\bar{u}_B = \bar{u}_A \frac{h_B}{h_A} \left(\frac{\mu_p}{\tau_y}\right)_A \left(\frac{\tau_y}{\mu_p}\right)_B \tag{5.13}$$

The following analysis is used as a guideline for altering the laboratory parameters such that the velocity profile from the field values in table 5.1 matches the velocity profile from the laboratory case.

5.2.2 Bingham Plastic Fluid Design

When beginning the pursuit of a suitable fluid for the experiments, there were several important properties that needed to be found. In search of a Bingham plastic fluid, it had to have both a yield stress and a nearly linear plastic viscosity to fit the field data and the Bingham plastic rheology model. Images were to be captured 8,5 centimeters into the flow channel, which meant that the fluid would have to be transparent as well.

Rheological testing on the Fann VG 35 rheometer showed promising results for several fluids with different additive concentrations. The drawback of this rheometer is that it is primarily designed for field purposes and will only give a very rough estimate of the rheological parameters of a fluid. For instance, finding the plastic viscosity and yield point of a fluid with this rheometer is carried out by the following equations:

$$PV = \theta_{600} - \theta_{300} \tag{5.14}$$

$$YP = \theta_{300} - PV \tag{5.15}$$

If we investigate these equations we see that the plastic viscosity and yield point is only calculated using two points, which does not give reliable results for a precise rheological behavior for a fluid. Although the Fann VG 35 was used regularly, it was only utilized to give a rough estimation of the fluid rheology. The Anton Paar rheometer were used for precise measurements.

An extensive amount of time was used testing different fluids. Many of which were discarded due to lack of transparency or not showing signs of a yield point. All chemicals were added to water to form a solution for testing. Below is a list of the additives that were studied.

- Xanthan Gum (XG)
- Carboxymethyl Cellulose (CMC)
- POLYPAC ELV
- POLYPAC A
- POLYPAC B
- DUOTEC
- Carbopol Ultrez 10

These chemicals were tested both separately and in combination with one another. For example, POLYPAC A were tested with DUOTEC. The first additive that was investigated was XG. This showed promising rheological properties with regards to YP when tested on the Fann VG 35, but was discarded later on due to not being transparent enough for PIV. The color of the solution was light yellow as seen in figure 5.16 and PIV recordings on this would be impossible. CMC was also discarded due to the same reason. POLYPAC ELV (extra low viscosity) showed to have too low viscosity. The additive which showed the most promising results considering transparency was POLYPAC A. Rigorous testing of the POLYPAC A was conducted. However, we were not able to procure additional batches of this additive, as it was an expired product from the supplier. We were forced to move on to a stronger version, POLYPAC B in order to proceed with the experiments. One downside keeping to these kind of products is that they are both proprietary products, meaning the exact composition is not listed on the product container. From this point on, POLYPAC B will be referred to as PAC (Polyanionic Cellulose).

Figure 5.16: PAC 0,2 wt% (left) and XG 0,67 wt% (right).

PAC was first tested on the OFITE Model 800 viscometer, as previously discussed in chapter 3.3.1, functions in the same way as the Fann VG 35. Rheological readings were also done for PAC on the Anton Paar rheometer. Figure 5.17 displays the results of 0,35 wt% solution of PAC on both the OFITE rheometer and Anton Paar. The CSR was executed on the Anton Paar.

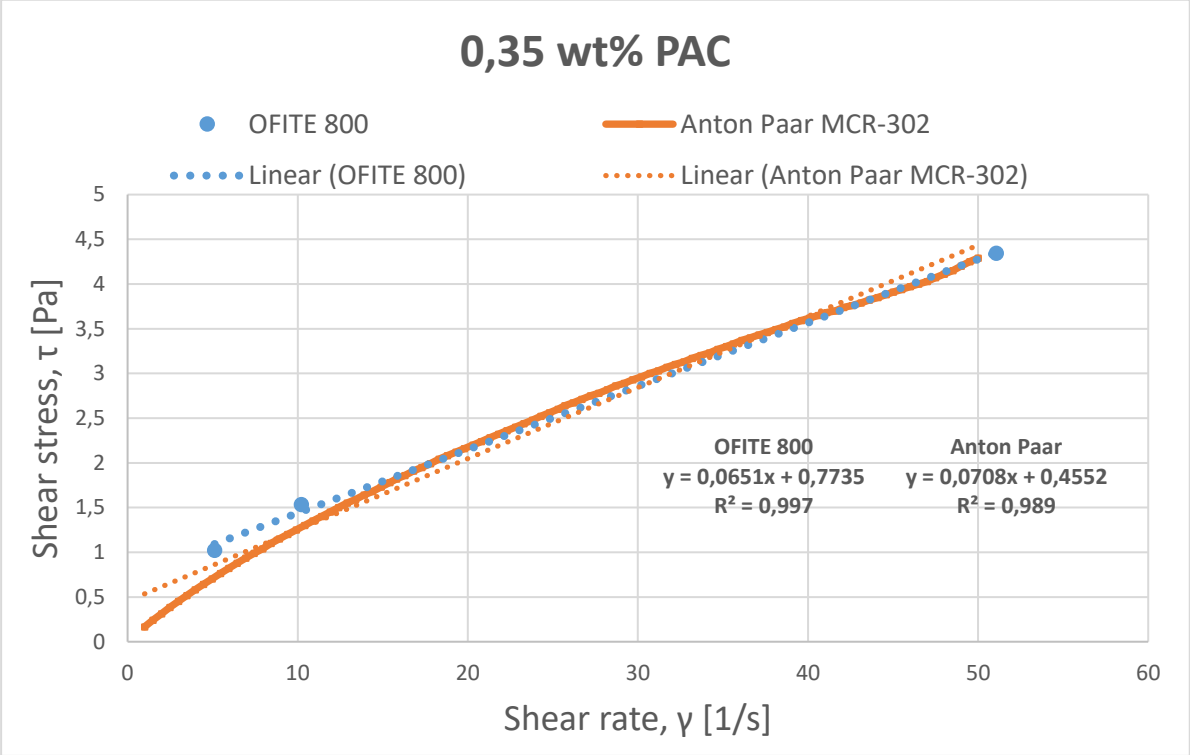

Figure 5.17: OFITE 800 and Anton Paar readings of 0,35 wt% PAC.

The regression results from the Anton Paar software is shown in the table below.

Table 5.4: Regression results from Anton Paar.

Parameter	Value	Unit
PV	0,758	Pa.s
YP	0,607	Pa
R^2	0,989	Dim.less

Although the PAC did not show a clear YP from the rheology tests, its regression was promising from both the Anton Paar readings and OFITE. In lack of any substitute additives at that time of experimentation, it was decided to go forth with the PAC for PIV experiments in hope of discovering the plug region that a Bingham plastic fluid is assumed to display.

By inserting the PV and YP from the regression results in table and the field values for PV and YP from table 5.1 into equation (5.13) we find the resulting velocity for laboratory conditions:

$$\bar{u}_B = 1\ m/s \frac{1{,}7\ cm}{3{,}33\ cm} \left(\frac{0{,}02}{5{,}75}\right)_A \left(\frac{0{,}57}{0{,}0681}\right)_B$$

$$\bar{u}_B = 0{,}015\ m/s$$

Which is equal to a flowrate of $q = 2{,}58\ lpm$ for the dimensions of our duct. The velocity of the field case is calculated by dividing the flowrate of 1750 lpm by the annular cross section.

Unfortunately, the PIV experiments did not yield any plug region and several modifications were attempted on the PAC in hope of introducing a clearer yield point, if any. As adding XG showed to give higher YP both by own rheological testing and by [52], some XG was added to a solution of PAC. This was quickly discarded, as even a quarter amount of XG compared to the amount of PAC, would make the solution not transparent enough for the PIV experiments. NaCl was also added as it was shown to increase the yield point of a fluid [54]. Although the solution became more transparent, adding NaCl to PAC yielded the complete opposite results as NaCl broke the polymer chains in the PAC which again resulted in less viscosity. NaCl will only increase the viscosity if it is allowed to react with clay minerals (Barite). Figure 5.18 shows the three solutions presented in the text above.

Figure 5.18: PAC 0,2 wt% (left), PAC 0,2 wt% + 3,0 wt% NaCl (middle) and PAC 0,2 wt% + 0,05 wt% XG (right).

All solutions were carefully mixed at slow rate to secure properly mixing and hydration of the additives. Several solutions were also left for days to settle before additional rheology tests were conducted to check for thixotropy and changes in transparency.

The CSS test first came to our attention after running the PAC in the loop and altering it with several other additives. Figures 5.19 and 5.20 shows that neither of the solutions contain any yield point what so ever.

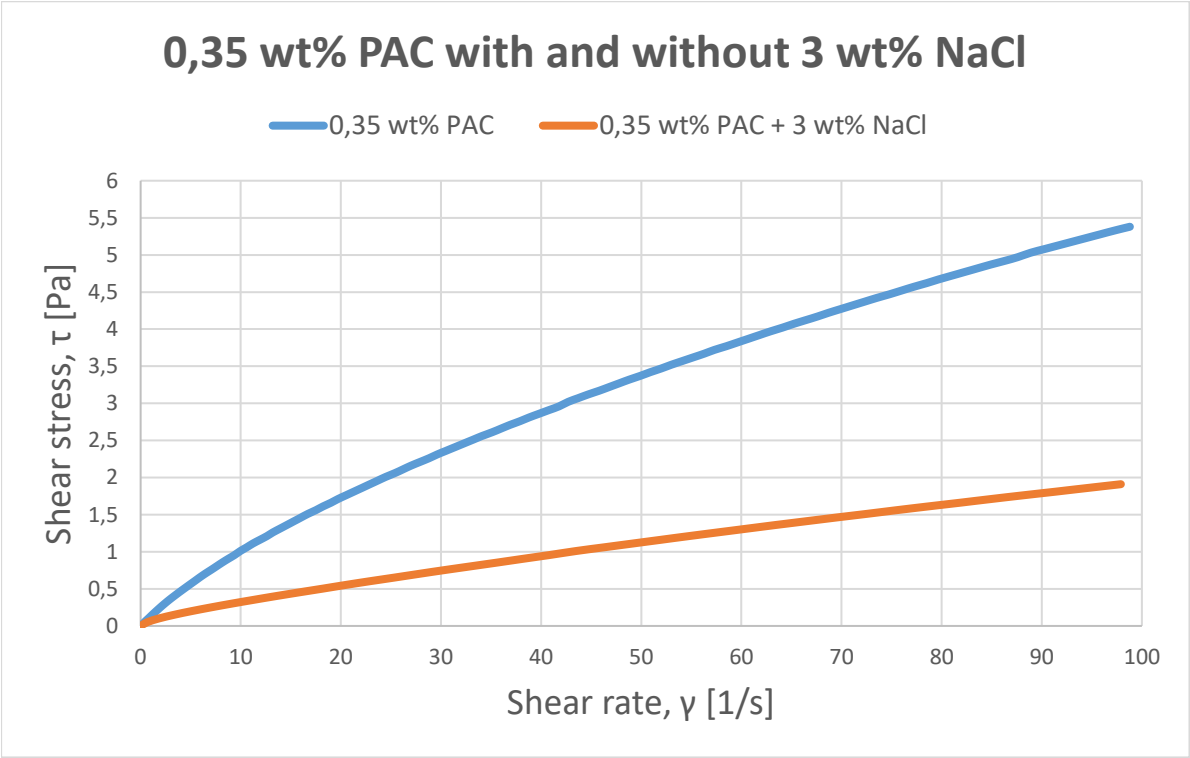

Figure 5.19: 0,35 wt% PAC with and without 3,0 wt% NaCl tested on CSS test.

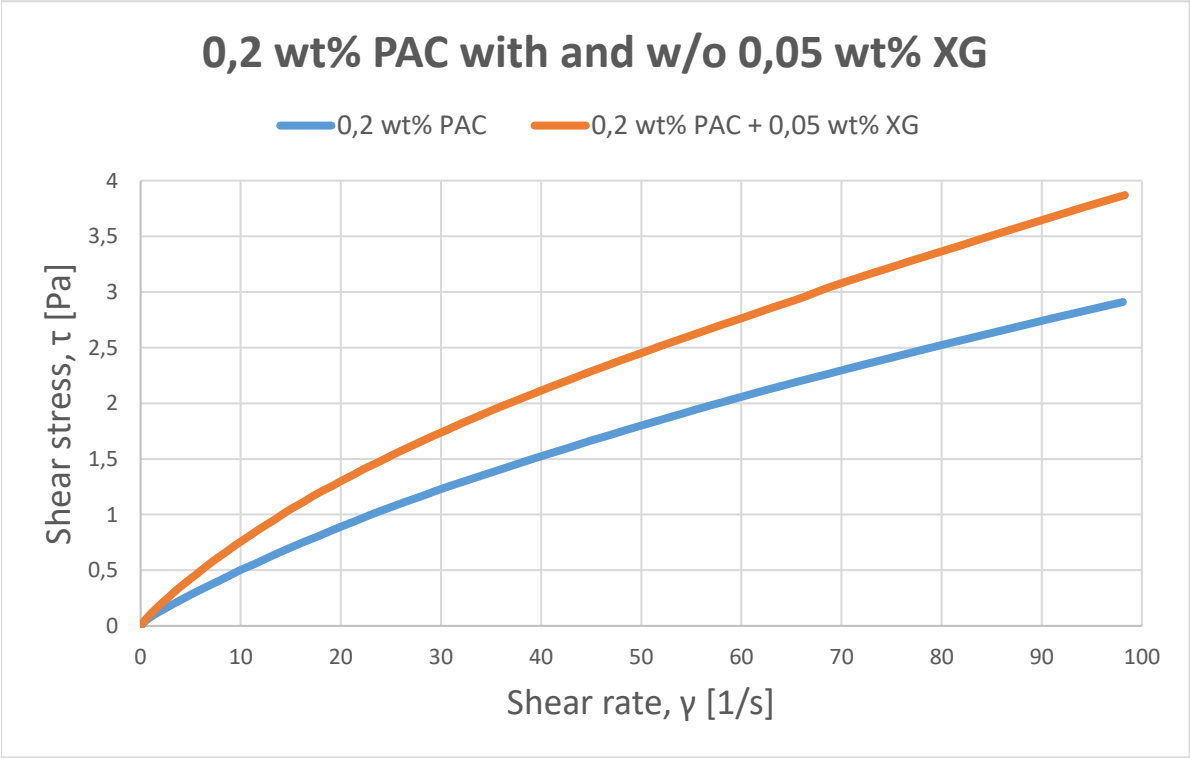

Figure 5.20: 0,2 wt% PAC with and without 0,05 wt% XG tested on a CSS test.

As all solutions up to this point has either been discarded due to non-transparency or not showing a yield point, one additive remains unpresented. Carbopol Ultrez 10 (Carbopol) was

the last additive tested out, as it was expensive and needed to be procured abroad. Although it was last in line, it was a solution that showed very promising results with regards to rheology. Carbopol is a crosslinked polyacrylic acid polymer which is also shown to be non-thixotropic [55].

Mixing Carbopol to form a yield stress fluid is a delicate process. The fine Carbopol powder has to be dispersed in a water solution before neutralized with an alkaline solution to thicken the fluid and produce a yield stress. The yield stress will be present at a pH approximately between 5 and 9. The mixing procedures is as follows and time at each step is dependent on the volume solution prepared. For a 10 L bulk solution, the Carbopol powder is mixed into water at a constant rate of 500 RPM. Once all the powder is properly dispersed, the solution is allowed to further mix for 7 hours to ensure complete hydration of the polymer and to let air bubbles within the solution to rise to the surface. The solution is then left over night for around 12 hours to allow all air and any residual foam to escape. It is critical to allow any air to disappear before the solution is neutralized. Once a neutralizing agent is added, the solution will develop a yield stress which can trap air bubbles inside the fluid. The fluid is neutralized with a premade 18 wt% sodium hydroxide (NaOH) solution. NaOH is added until the fluid reaches a pH of around 7,0 [56]. A smaller laboratory sample does not require the large amount of time to prepare as a 10 L bulk preparation. For example a 500 ml solution can be prepared with gentle magnetic agitation at 1000 RPM for 15 minutes in order to allow the Carbopol to fully disperse. The solution is then left static for 30 minutes for hydration before neutralizing with NaOH at 1000 RPM agitation. Letting it rest for around one hour before doing rheology tests is recommended [57].

Figure 5.21: Carbopol dispersed in water after 30 min (left). Condition of the solution after 7 hours agitation (middle) and solution left static for 12 hours (right) before neutralization.

The Carbopol presented in figure 5.21 was also run through the constructed flow loop to visually verify if it would be fit for PIV purposes. It was observed that air bubbles were introduced to the fluid while running it through the system. As discussed above, when air bubbles enter the fluid, they can be exceedingly difficult to remove and will result in poor PIV images. This is why PIV cannot be conducted on the fluid before a solution is found to mitigate the air contamination in the current system configuration. Possible solutions to this is discussed in future work under chapter 9.

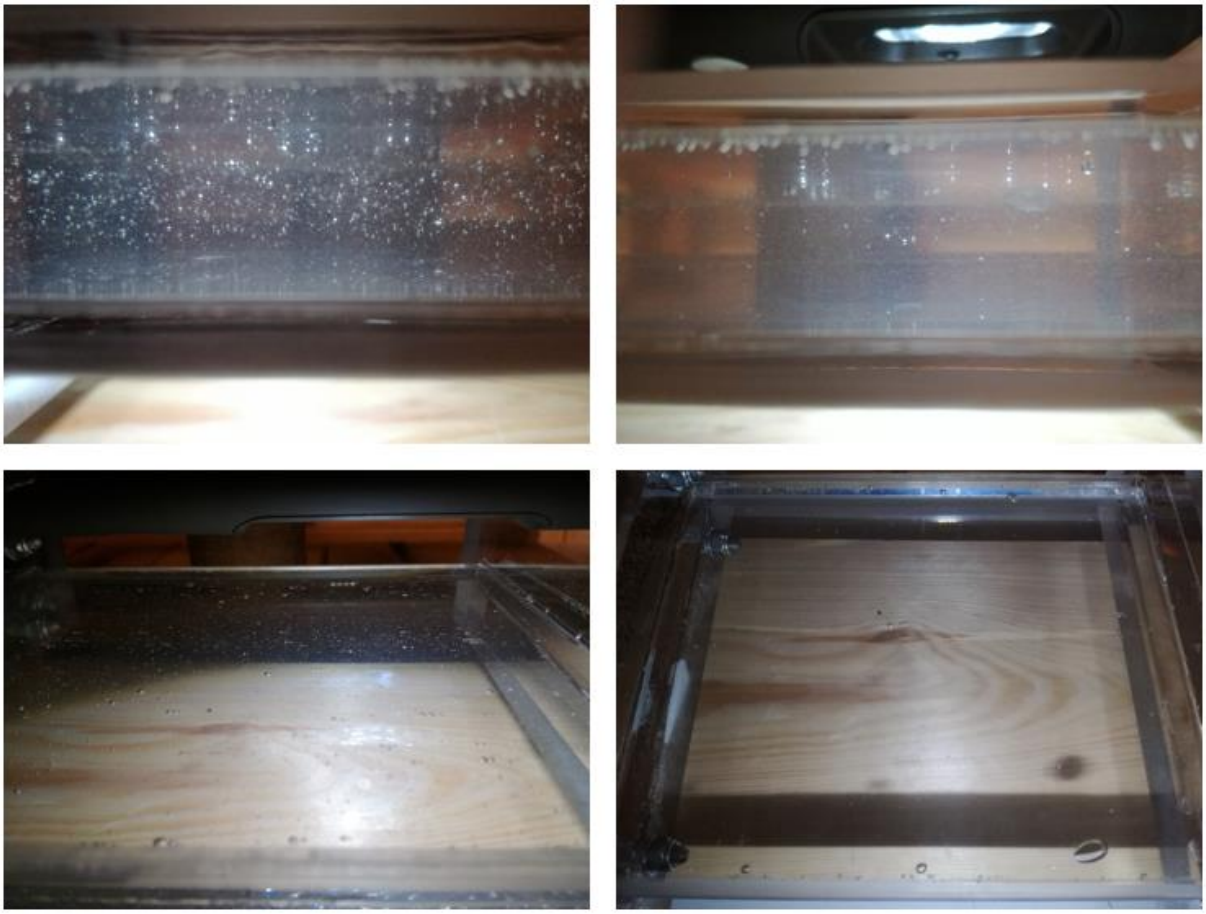

Figure 5.22: Carbopol in flow channel (left). Condition after leaving it static in the channel for 24 hours (right).

The rheological results of 0,1 wt% Carbopol solution from the CSS test on the Anton Paar in presented in the figure 5.23.

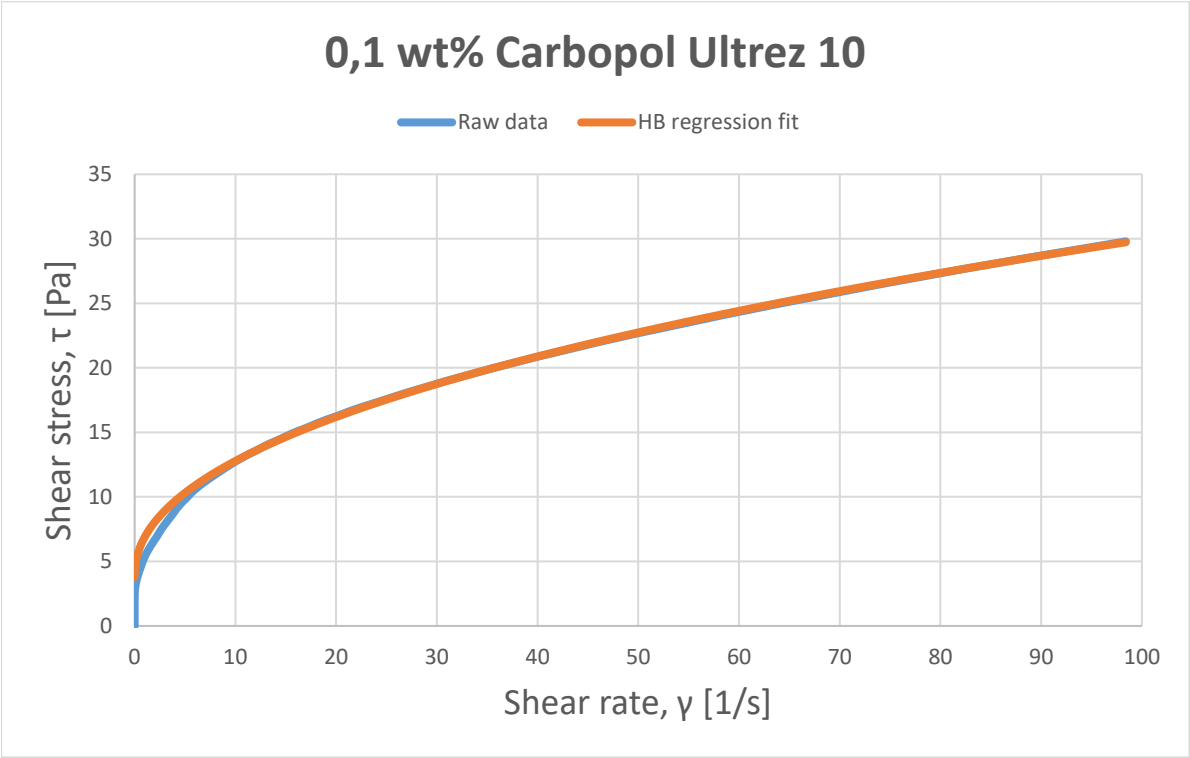

Figure 5.23: 0,1 wt% of Carbopol raw data and Herschel-Bulkley regression fit.

The graph presented here shows the rheology of the 0,1 wt% Carbopol solution. As seen it does not present a typical Bingham plastic curve, but rather a Herschel-Bulkley (HB) behavior. The HB is a three-parameter rheology model, which can be described mathematically the following equation.

$$\tau = \tau_0 + K\gamma^n \tag{5.16}$$

Where τ is the shear stress, τ_0 is the yield point, K is the consistency index, n is the flow behavior index and γ is the shear rate.

The blue curve is a HB regression fit with the values presented in table 5.5 together with the shear rate collected from the raw theology data.

Table 5.5: HB regression values from Anton Paar software

Parameter	Value	Unit
τ_0	3,7989	Pa
K	3,0887	Pa.s
n	0,4637	Dim.less
R^2	0,9999	Dim.less

From figure 5.23 and the correlation ratio in table 5.5 we can see that it is almost a perfect fit for the HB rheology model. Even though we originally were after a fluid fitting the Bingham plastic rheology model, this fluid is a good candidate. Whether this fluid will make an acceptable fit for our scaling methodology by using the Bingham number will be presented in chapter 6.

5.3 Experimental Procedures

Before continuing presenting the PIV results it is important to introduce the experimental procedures and practices that were implemented both prior to and during the time of experimentation. As the experiments involved a 200 mW laser, special HSE precautions were facilitated and an HSE course regarding usage of lasers needed to be completed before conducting PIV experiments by oneself. In order to prevent access from non-participants during PIV experiments, the room had to be isolated such that reflected laser light would not escape the room. One can see in the pictures below that the windows of the room had been covered and a laser warning sign is attached to the door. Two red flashing light were also located outside the room while the laser is operated, in order to alert others working outside the room.

Figure 5.24: Outside the room where the PIV experiments were conducted.

The experiments were conducted under strict behavior. Laser protection googles, which block out the specific laser wavelength of 532 nm were worn at all times while the laser was on. The experimental work was also never done alone, in case of accidents as the laser beam can permanently damage ones vision if it gets into the eyes.

The experimental procedures leading up to image acquisition are explained stepwise in the list below:

1. The flow channels were lined up and flanged together.
2. The mid-point of the duct was measured up at the location of the channel where the laser was to be installed. This was used as a reference point when the laser was turned on.
3. The fluid hoses were connected to the duct and the pump was activated.
4. In order to mitigate air bubbles while flooding, the flow channel was tilted at about a 45-degree angle so the fluid inside the duct could swipe the inside surfaces and carry the air bubbles to the exit.
5. When the flow had stabilized at the desired flow rate setting, the PIV equipment was set up.
6. The laser was placed at the correct position and lined up with the premade reference point. It is important to have the laser plane falling down at a 90-degree angle to minimize the chance of seeding particles moving in and out of the plane. A box was placed around the laser in order to reduce light reflection.
7. The camera was positioned and connected to a computer for image acquisition.

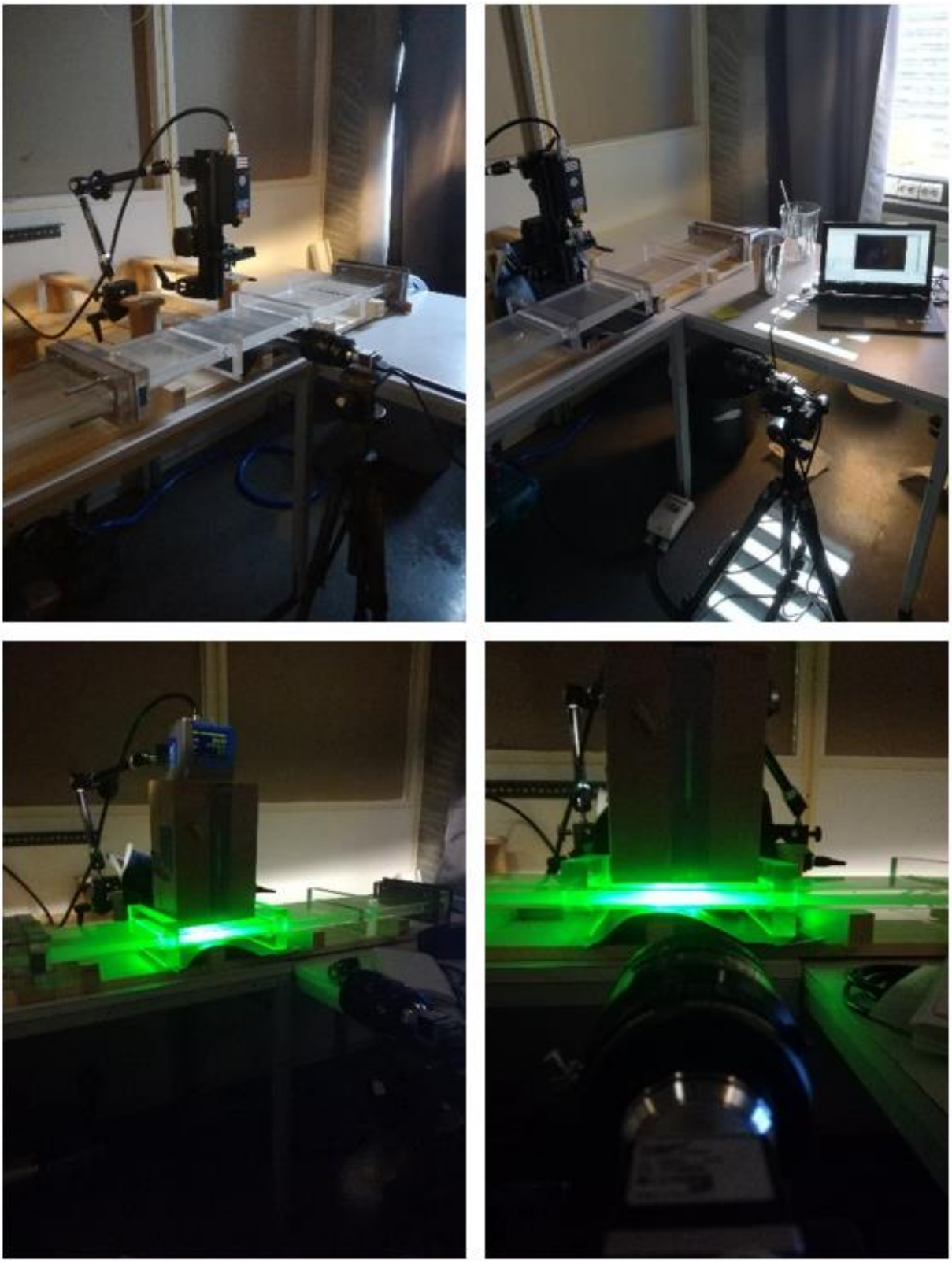

Figure 5.25: PIV setup showing the flow channel, laser, camera and computer in place.

Vortices and eddies were seen at along the first channel, up to about 50 centimeters for the highest flowrate that was tested out. The stability length was studied visually prior to PIV experiments for the current setup and was determined to be at approximately 125 centimeters down the channel, which is where the PIV experiments were conducted. No entry effects were visually spotted at this point.

5.3.1 Image Acquisition and Post-Processing Procedures

After setting up the camera and connecting it to the computer, the image had to be configured to be in focus at the right distance from the duct. Before acquiring images, parameters such as the f-number on the lens, exposure time, and image acquisition frame rate had to be set at the right values. The intensity on the laser sheet was also a factor. Pylon Viewer was the software used to record the PIV images

Seeding particles were added continuously to the flow until an acceptable amount could be seen on the computer. One hundred images were acquired on each run, with varying frame rate and exposure time. Pre- and post-processing were done on every run with different configuration to investigate which gave the best vector and velocity profile calculations. PIVlab, which is a MATLAB based, open-source PIV software, was used for the image processing. PIVlab also offers an easy to use GUI (Graphical user interface) [37, 38, 39].

The procedures from acquisition of the raw images to finally resulting in a velocity profile will now be explained in simple steps.

1. First the raw images are imported into PIVlab and a sequence style of 1-2, 2-3 etc. is chosen, meaning image A is compared to image B and B is compared to image C etc.
2. The raw PIV images are presented.
3. The region of interest is chosen and masks can be added if there are region one wishes to exclude.
4. Pre-processing interface where CLAHE and high pass filter has been chosen at suitable values.
5. The PIV algorithm with FFT window deformation for more accurate results is chosen. Multiple pass interrogation with decreasing interrogation windows are also selected here.
6. Analysis and vector calculation of the images are initiated. Time taken to compute depends on choice of correlation, window deformation interpolator, the sub-pixel estimator and, of course the number of images.

7. Vector limits are chosen. As we are only interested in the positive u-component, we exclude negative u-components.
8. Green vectors are the ones which are calculated and orange vector are interpolated ones. Standard deviation and local median filter can be included here. Also, rejection of erroneous vector can be manually rejected. Only a small number of interpolated vectors are visible here in the upper left and right corners.
9. A reference distance is drawn onto the image and time step between each image taken is inserted so PIVlab can display values in metric units.
10. Among other choices at this point, the images can be smoothened using the Gaussian kernel method. An image containing the mean value of all vectors can also be include here.
11. A poly line is drawn to extract the velocity profile of the u-components is executed here.
12. The velocity profile in extracted from the poly line and plotted.

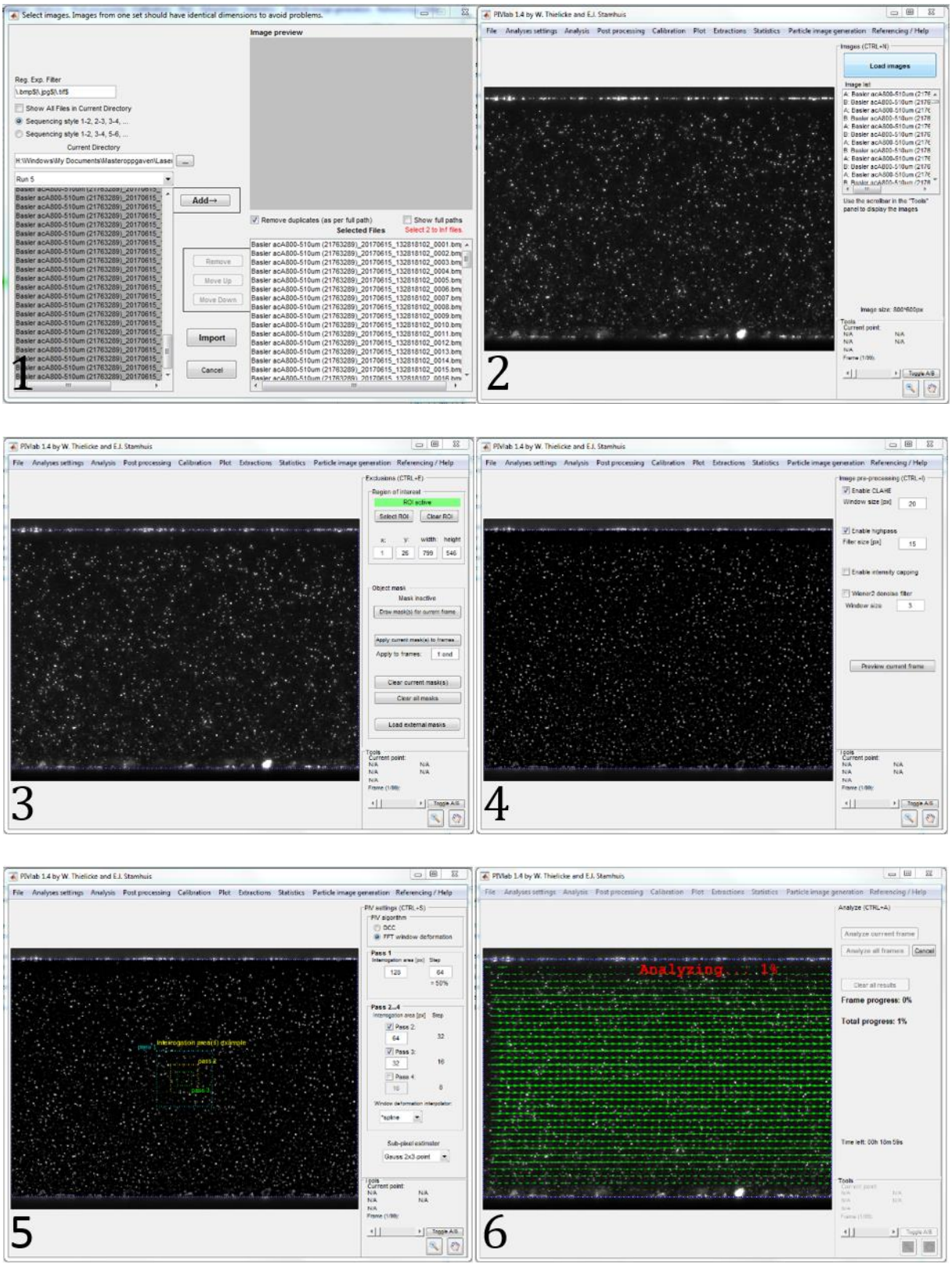

Figure 5.26: Image post-processing procedures step 1-6 [37, 38, 39].

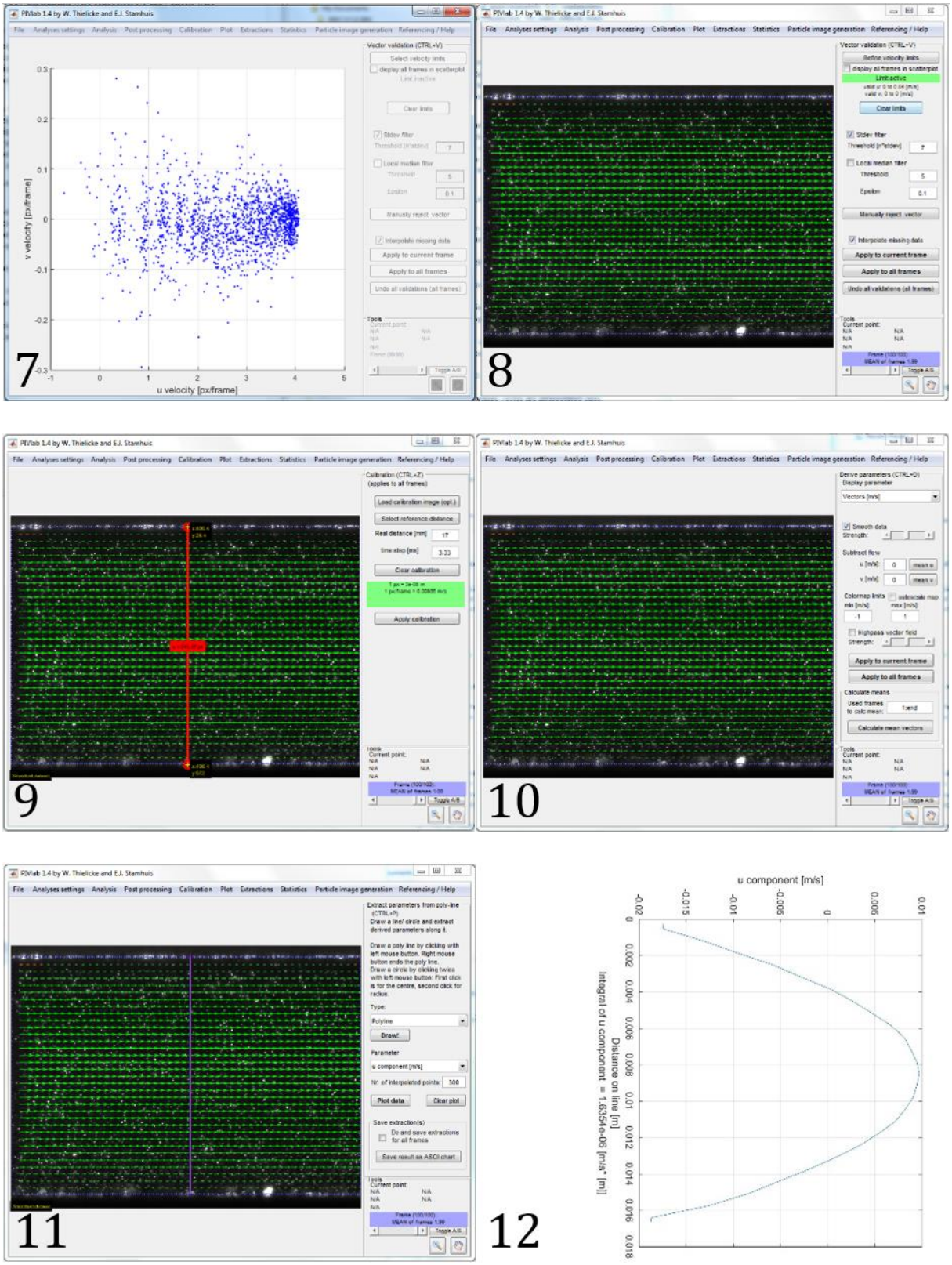

Figure 5.27: Image post-processing procedures step 6-12 [37, 38, 39].

6 Results

This chapter is dedicated to display the results from the PIV experiments for the Newtonian fluid and validation of the Carbopol. Firstly, the velocity profile generation of the raw experimental PIV data together with the theoretical Newtonian profile is presented. This was done in order to experimentally show if our theoretical verification of the channel aspect ratio of 1:10 is acceptable. Secondly, the rheological results of the Carbopol is utilized to see whether this fluid is acceptable to use in our Bingham number scaling procedure is also presented. Discussion of the results and obstacles while completing this thesis are presented in chapter 7.

6.1 Theoretical and Experimental Profile Comparison

The data points from the velocity profiles in PIVlab were extracted and plotted in separate figures in EXCEL. The experimental velocity profiles were then matched with the theoretical profiles two several flowrates for the Newtonian fluid. As the Gardena flowrate measurement device was not a reliable enough system at the time of experimentation, the flowrate was obtained from the PIV measurements by reading the u_{max} value from the raw data points. This value was then used as an input in equation (3.30) to obtain the average experimental flowrate. The calculated average flowrate was then used as an input in equation (3.28) to yield the theoretical profile for that specific flowrate. The theoretical and experimental profiles where then matched in the same plots.

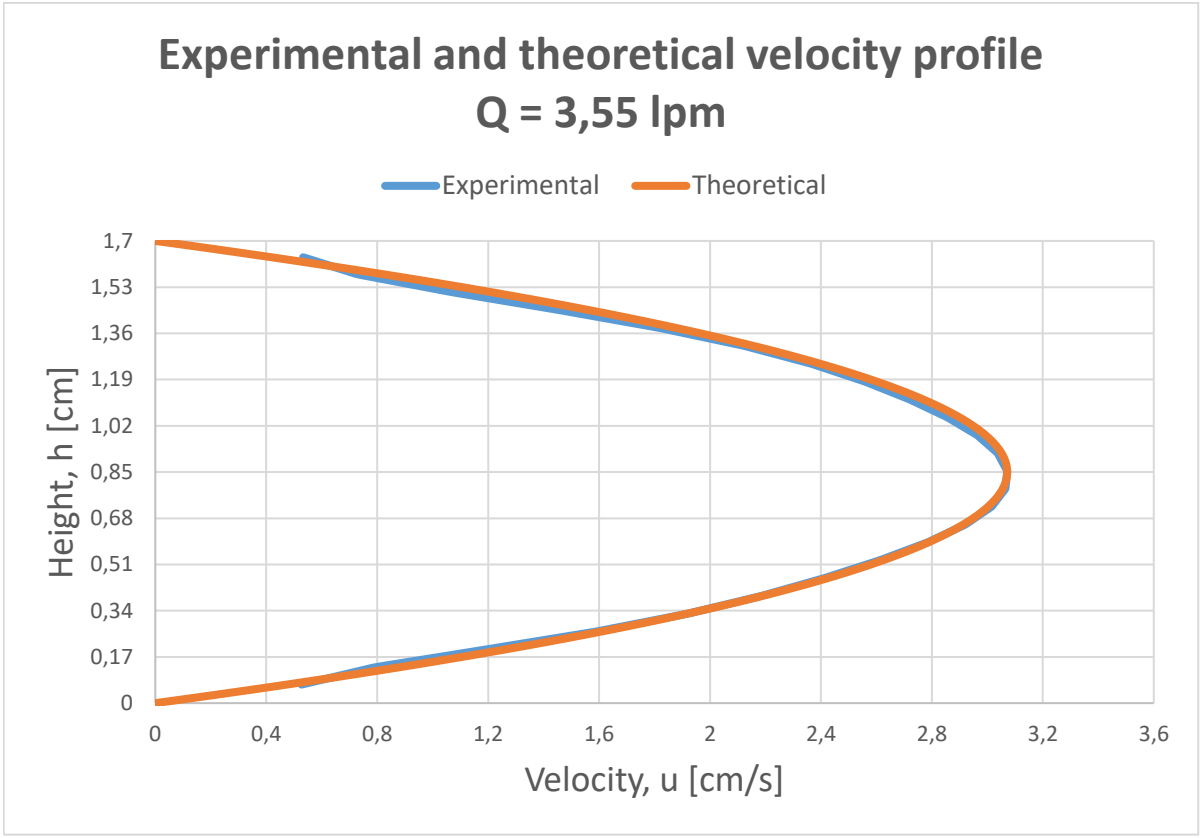

Figure 6.1: Experimental and theoretical velocity profile comparison at Q = 3,55 lpm.

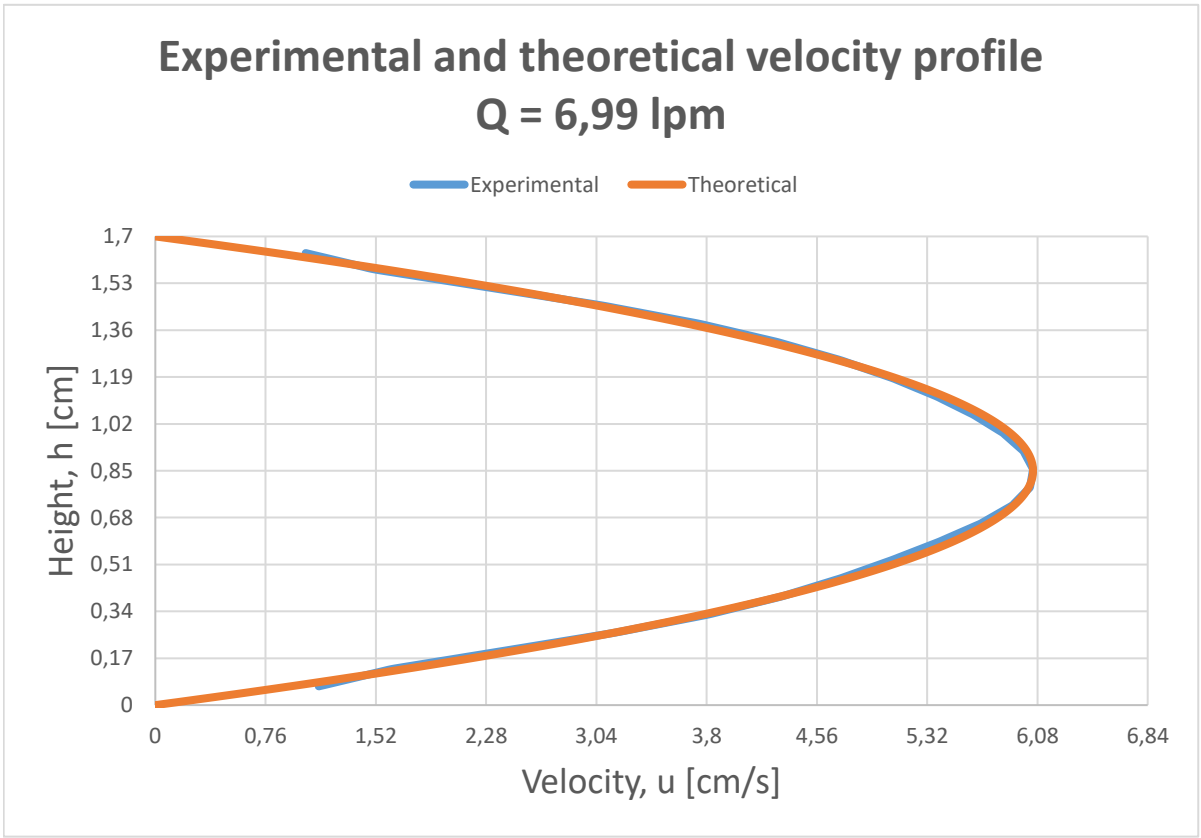

Figure 6.2: Experimental and theoretical velocity profile comparison at Q = 6,99 lpm.

From figure 6.1 and 6.2, the experimental velocity profiles show a satisfactory match when compared to the theoretical Poiseuille slot flow equation (3.24). However, two observations can be made. There are areas where the two curves do not completely overlap and the experimental curve is missing data points at the top and bottom, which is discussed in chapter 7.

6.2 Bingham Number Fit for Carbopol

As seen in figure 5.23, the Carbopol solution shows promising results for a PIV fluid with our requirements with regards to yield point and transparency. However, further investigation need to be conducted, as it is not a clear Bingham plastic fluid, but a HB fluid. As the HB rheology model also includes a yield point, such a fluid should also exhibit a plug region. One way to do this is by comparing the theoretical velocity profiles from both the Bingham plastic and HB regression results of the raw rheology data. The profile comparison is done using MATLAB with the values presented in table 5.5 and 6.1 for the HB and Bingham plastic profiles, respectively and plotted in figure 6.3.

Table 6.1: Bingham plastic regression values from Anton Paar software

Parameter	Value	Unit
τ_y	13,227	Pa
μ_p	0,299	Pa.s
R^2	0,988	Dim.less

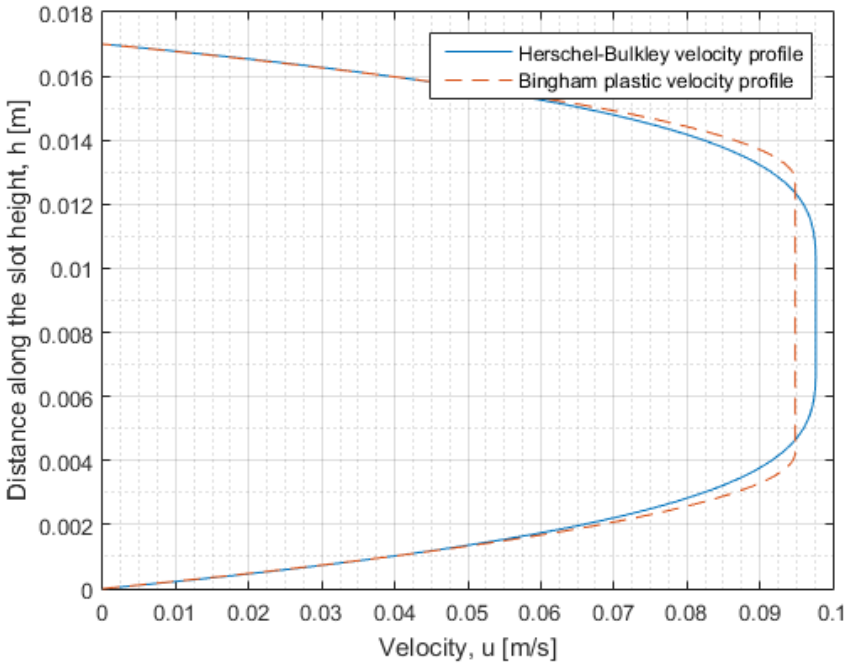

Figure 6.3: Velocity profile plot of regression results of HB and Bingham plastic fit.

Figure 6.3 shows an acceptable comparison, although it deviates both in the profile peak and plug region height. We can also see that the HB plug region is more rounded off than the Bingham plastic.

The circulation efficiency depends on the shear rate for both a Bingham plastic and a HB fluid. A smaller shear rate will result in a higher circulation efficiency. The plug region is where the fluid is remained unsheared and therefore, a larger plug will yield a better circulation efficiency [58].

7 Discussion

This chapter can be divided into two parts of discussion. The first part will recall the physical side of the work laid down in this thesis, while the second part will discuss the results obtained in the thesis.

7.1 Physical Design and Implementation

Designing and constructing a laboratory equipment from the ground up was never thought of as a straight forward process and did, without a doubt, pose several challenges. In many ways, the practical work was more of a trial and error process to investigate what functions and what serves merely as a setback.

The first objective was to manufacture the flow channel and design the setup of the flow loop. Several parts of the current flow loop was equipment that was easily and already available at the university or could be purchased without too much cost. A good amount of time and work was invested in building and configuring the flow loop and reconstructing the room assigned for PIV purposes. Both the windows and the roof of the room had to be covered such that outside light would not disturb the PIV experiments.

The flow loop began with a simple 20 centimeter long glass channel. Glass was first chosen as it had excellent optical properties. During trail flow tests, the pressure inside the glass channels would result in numerous amount of leakages at the glued sections. Two glass channels were tested out in the early stages of this thesis. However, due to leakages and fragility of the glass when being flanged between the acrylic channels, the use of glass was discarded all together.

The acrylic material which is now at use, seemed to give just as good optical properties for PIV experiment without going into the physics of optics.

Several pressure mitigation solutions were implemented as one of the acrylic channels bursted during flow testing.

One of the acrylic channels bursted during flow testing due to large pressures. Before implementing a solution, a detailed pressure calculation along the whole system was conducted. The start and endplate was then configured with three holes each fitted with ¾ inch nipples. The solution applied to the flow loop showed to mitigate the pressure more than sufficient as the flow would now have difficulties to fill up the entire cross sections of the outlet hoses.

The flow loop, as it stands, is the best solution till now and is fully fit for PIV experiments, but has still much room for improvements. When filling the duct, it is lifted up to let the fluid drag any air bubbles along the wall to the outlet in order to reduce the air in the system. Another, simpler solution should be made here, although it is unsure if the whole system is air tight as air was seen to be introduced to the system when flowing both PAC and Carbopol. It is worth mentioning that air would be easier trapped in a more viscous yield stress fluid than water and difficulties regarding this was foreseen. Whether it is the piston pump or any of the several hose connections that it not fully sealed remains to be found out. Improvements regarding the physical flow loop will be mentioned in chapter 8.

Before conducting the PIV experiments, a laser HSE course was needed to be completed. This delayed the PIV experiments a little, but was of great importance to understand the danger related to operating a 200 mW laser. In addition to this, the vast field of PIV needed to be studied and understood in order to know how to achieve good quality images.

Both the physical design of the flow channel and fluid design were done side by side. Finding an appropriate yield stress fluid for the experiments was a long and time consuming search. Although Carbopol was discovered in a quite early stage, it was decided to move forth with PAC as this was showing an acceptable rheological result at that time. However, the CSS test showed clearly that PAC was not a yield stress fluid, but instead a Power law fluid. In hindsight, Carbopol should have been tested out earlier as literature refers to it as a transparent yield stress fluid, which was exactly the requirements for our fluid. Anyhow, the right fluid is now discovered and will be used for further work when air bubble mitigation solutions are found.

7.2 Experimental Results

The first objective of this thesis was to design a flow duct, utilizing the slot configuration method of a concentric annulus and downscaling of field size dimensions. Investigation of which aspect ratio the side wall effects can be negligible, such that the flow equations for an infinite wide duct can be used to calculate the theoretical velocity profile 8,5 centimeters into the channel was also part of this objective. This was achieved by studying three different references, two for a Newtonian case and one for a Bingham plastic case. Experiments for a Newtonian fluid were conducted to verify the concluded aspect ratio from chapter 5.1.

From figure 6.1 and 6.2 we can see that comparing the theoretical and experimental Newtonian profiles reveals a good overall match. Still, there are two remarks that can be made. Why the curves do not completely overlap can be a result of different factors which are unknown at the

time, but can be speculated. Among several other things, it can include post-processing techniques and values or out of plane seeding particles which generate errors in vector calculations. The reason for the incomplete experimental curve is lack of data points and seeding particles at the top and bottom wall. Few seeding particles at the top can be caused by gravitational forces, although these should be negligible as the seeding particles are neutral buoyant in water and the effect of gravity should not have a large impact along the length of the channel. Another reason for missing data at top and bottom could be a result of particle repulsion from the walls.

The second objective of this thesis was to identify a transparent yield stress fluid suitable for PIV experiments in the designed duct. In addition to this, the fluid would also have to be applicable to our Bingham number similarity scaling method from field to laboratory conditions. In spite of showing a HB behavior rather than a Bingham plastic, the most suitable fluid found at this point is Carbopol.

The comparison of the regression results of Carbopol for the HB and Bingham plastic rheology models done in MATLAB for figure 6.3 displays that the curves are well within 10% of each other. The difference in the plug region height and velocity peak is of course a result of the definition of the two rheology models.

8 Conclusion

Considering the objectives of this thesis and the methods used to arrive at a conclusion, all goals were achieved. Two analytical solutions for a Newtonian case together with one for a Bingham plastic case were presented to study the adequate aspect ratio for the designed duct. All of which verified that an aspect ratio of 1:10 would be theoretical sufficient. The experimental velocity profiles for the Newtonian fluid are also in compliance with the theory.

Carbopol is shown to serve as a good solution for the transparent yield stress fluid and can be utilized further for PIV experiments when the air bubble issue is resolved. Although it better fits the Herschel-Bulkley rheology model, it can be used in the Bingham number similarity scaling method, according to figure 6.3.

9 Future Work

As mentioned in chapter 7, the flow loop as it stand has great room for improvements. It also the potential to be configured to study more than just the velocity profiles in a concentric annulus. Improvements to the system and suggested future work is presented in the following points:

- In order to eliminate air entering the system at any point, the whole system should be thoroughly checked again. An isolated system would be optimal.
- As it is unsure if it is the pump that introduces air into the system, this should be checked and possibly be replaced by a more suitable pump, such as screw, progressive cavity or gear pump.
- Centrifuging has shown to remove air bubbles in a yield stress fluid [59].
- Since there were now reliable flowrate measurement system in the flow loop, a flowmeter of the Coriolis or ultrasound type should be implemented.
- A more convenient way of elevating the duct while flooding, e.g. by incorporating a pulley or a mechanical system.
- Configuring a half automated system where laser intensity, camera acquisition parameters and flowrate can be changed from a computer. LabVIEW is a software where this can be applied.
- Include an irregular wellbore geometry such as a washout zone of desired size and shape. An eccentric annulus could also be studied, but requires a new channel with a curved shape to be manufactured.
- Study circulation efficiency for a regular and irregular wellbore geometry by either adding dye or seeding particles to the displacing fluid while keeping the stationary fluid pure.
- Study displacement efficiency for a regular and irregular wellbore geometry with a two fluid setup.
- This will all be assessed in the SPE paper [1].

References

[1] Divyankar, S., Berntsen, K., Skadsem, H. J., Aasen, J., *Mud Displacement in Washout Section Prior to Cementing for Improved Annular Zonal Isolation*, in *Abu Dhabi International Petroleum Exhibition and Conference Submission*. 2017, SPE-188777-MS in press: Abu Dhabi.

[2] Nelson, E.B. and D. Guillot, *Well cementing*. 2nd ed. 2006, Sugar Land, Texas: Schlumberger. p. 1.

[3] PetroWiki. *Cementing operations*. [Cited 2017 03.04.17]; Available from: http://petrowiki.org/Cementing_operations.

[4] Nelson, E.B. and D. Guillot, *Well cementing*. 2nd ed. 2006, Sugar Land, Texas: Schlumberger. p. 514-514.

[5] Jones, P.H. and D. Berdine, *Oil-Well Cementing*. American Petroleum Institute.

[6] Nelson, E.B. and D. Guillot, *Well cementing*. 2nd ed. 2006, Sugar Land, Texas: Schlumberger. p. 143-145.

[7] Nelson, E.B. and D. Guillot, *Well cementing*. 2nd ed. 2006, Sugar Land, Texas: Schlumberger. p. 145.

[8] Nelson, E.B. and D. Guillot, *Well cementing*. 2nd ed. 2006, Sugar Land, Texas: Schlumberger. p. 148-150.

[9] Rønningsen, H.P., *Rheology of Petroleum Fluids.* Annular Transaction of the Nordic Rheology Society, 2012. **20**.

[10] Stavanger, U.o., *Øvinger i Bore- og Brønnvæsker (PET 210)*. 2014. p. 112.

[11] Okafor, M.N., J.F. Evers, *Experimental comparison of rheology models for drilling fluids.* SPE, 1992.

[12] Mezger, T.G., *The Rheology Handbook: for users of rotational and oscillatory rheometers*. 3rd rev. ed. ed. European coatings tech files. 2011, Hannover: Vincentz.

[13] Mezger, T.G., *The Rheology Handbook: for users of rotational and oscillatory rheometers*. 3rd rev. ed. ed. European coatings tech files. 2011, Hannover: Vincentz. p. 51

[14] Rommetveit, R., et al., *HPHT Well Control; An Integrated Approach*, in *Offshore Technology Conference, 5-8 May, Houston, Texas*. 2003, Offshore Technology

Conference.

[15] Nelson, E.B. and D. Guillot, *Well cementing*. 2nd ed. 2006, Sugar Land, Texas: Schlumberger. p. 95.

[16] Nelson, E.B. and D. Guillot, *Well cementing*. 2nd ed. 2006, Sugar Land, Texas: Schlumberger. p. 96.

[17] Muherei, M.A., *Common Versus Herschel-Bulkley Drilling Fluid Models: Effect of Their Rheological Parameters on Dynamic Particle Settling Velocity.* American Scientific Research Journal for Engineering, Technology, and Sciences, 2016. **16**(1).

[18] Nelson, E.B. and D. Guillot, *Well cementing*. 2nd ed. ed. 2006, Sugar Land, Texas: Schlumberger. p. 97.

[19] Nelson, E.B. and D. Guillot, *Well cementing*. 2nd ed. ed. 2006, Sugar Land, Texas: Schlumberger. p. 93-94.

[20] Munson, B.R., T.H. Okiishi, and D.F. Young, *A Brief Introduction to Fluid Mechanics*. 2nd ed. 2001, New York: Wiley. p. 246-249.

[21] Bourgoyne, A.T., Chenevert, Martin E., Millheim, Keith K., Young Jr., F. S., *Applied drilling engineering*. SPE textbook series. Vol. Vol. 2. 1986, Richardson, Texas: Society of Petroleum Engineers. p. 141-142.

[22] Bourgoyne, A.T., Chenevert, Martin E., Millheim, Keith K., Young Jr., F. S., *Applied drilling engineering*. SPE textbook series. Vol. Vol. 2. 1986, Richardson, Texas: Society of Petroleum Engineers. Appendix B.

[23] Adrian, R.J. and J. Westerweel, *Particle image velocimetry*. Cambridge aerospace series. Vol. 30. 2011, Cambridge: Cambridge University Press. p. 1-5.

[24] Raffel, M., et al., *Particle Image Velocimetry A Practical Guide*. 1998, Springer Berlin Heidelberg: Imprint: Springer. p. 1-6.

[25] Hoseini, A.A., *Experimental study of turbulent flow with dispersed rod-like particles through optical measurement*, in *Department of Energy and Process Engineering*. 2014, Norwegian University of Science and Technology. p. 20.

[26] Hoseini, A.A., *Experimental study of turbulent flow with dispersed rod-like particles through optical measurement*, in *Department of Energy and Process Engineering*. 2014, Norwegian University of Science and Technology. p. 18-19.

[27] Hoseini, A.A., *Experimental study of turbulent flow with dispersed rod-like particles through optical measurement*, in *Department of Energy and Process Engineering*. 2014, Norwegian University of Science and Technology. p. 18.

[28] Wikipedia. *Stokes Number*. 2017 [cited 2017 05.06.17]; Available from: https://en.wikipedia.org/wiki/Stokes_number.

[29] Adrian, R.J. and J. Westerweel, *Particle image velocimetry*. Cambridge aerospace series. Vol. 30. 2011, Cambridge: Cambridge University Press. p. 13-16.

[30] Dynamics, D. *Seeding Materials*. 2017 [cited 2017 28.05.17]; Available from: https://www.dantecdynamics.com/seeding-materials.

[31] Adrian, R.J. and J. Westerweel, *Particle image velocimetry*. Cambridge aerospace series. Vol. 30. 2011, Cambridge: Cambridge University Press. p. 167-170.

[32] Suwtech, I.-V. *DPGL-2200 L*. 2017 [cited 2017 01.06.17]; Available from: http://www.ii-vi-suwtech.com/products/DPSS-green-laser.html.

[33] Basler. *Camera Specifications*. 2017 [cited 2017 02.05.17]; Available from: https://www.baslerweb.com/en/products/cameras/area-scan-cameras/ace/aca800-510um/.

[34] Adrian, R.J. and J. Westerweel, *Particle image velocimetry*. Cambridge aerospace series. Vol. 30. 2011, Cambridge: Cambridge University Press. p. 7.

[35] Raffel, M., et al., *Particle Image Velocimetry A Practical Guide*. 1998, Springer Berlin Heidelberg: Imprint: Springer. p. 42.

[36] Adrian, R.J. and J. Westerweel, *Particle image velocimetry*. Cambridge aerospace series. Vol. 30. 2011, Cambridge: Cambridge University Press. p. 6-10.

[37] Thielicke, W., Stamhuis, E.J, *PIVlab – Towards User-friendly, Affordable and Accurate Digital Particle Image Velocimetry in MATLAB.* Journal of Open Research Software, 2014. **2** (1):e30.

[38] Thielicke, W., Stamhuis, E.J, *PIVlab - Time-Resolved Digital Particle Image Velocimetry Tool for MATLAB (version 7.10).* 2014.

[39] Thielicke, W., *The Flapping Flight of Birds - Analysis and Application*. 2014, Rijksuniversiteit Groningen.

[40] Hoseini, A.A., *Experimental study of turbulent flow with dispersed rod-like particles through optical measurement*, in *Department of Energy and Process Engineering*. 2014, Norwegian University of Science and Technology. p. 31.

[41] Sween, J.K., Cowen, E. A., *Quantitative imaging techniques and their application.* Advances in Coastal and Ocean Engineering, 2004. **9**: p. 1-49.

[42] Sælevik, G., *Particle image velocimetry applied to complex flows in a wave tank*, in *Faculty of Mathematics and Natural Sciences*. 2009, University of Oslo: Oslo.

[43] Wereley, S.T., Meinhart, C. D., *Second order accurate particle image velocimetry.* Experiments in Fluids, 2001. **31**: p. 258-268.

[44] Adrian, R.J. and J. Westerweel, *Particle image velocimetry*. Cambridge aerospace series. Vol. 30. 2011, Cambridge: Cambridge University Press. p. 393-397.

[45] Scarano, F., *Iterative image deformation methods in PIV.* Measurement Science and Technology, 2002. **13**: R1-R19.

[46] Adrian, R.J. and J. Westerweel, *Particle image velocimetry*. Cambridge aerospace series. Vol. 30. 2011, Cambridge: Cambridge University Press.

[47] Raffel, M., et al., *Particle Image Velocimetry A Practical Guide*. 1998, Springer Berlin Heidelberg: Imprint: Springer.

[48] Bourgoyne, A.T., Chenevert, Martin E., Millheim, Keith K., Young Jr., F. S., *Applied drilling engineering*. SPE textbook series. Vol. Vol. 2. 1986, Richardson, Texas: Society of Petroleum Engineers. p. 141-142.

[49] Bourgoyne, A.T., Chenevert, Martin E., Millheim, Keith K., Young Jr., F. S., *Applied drilling engineering*. SPE textbook series. Vol. Vol. 2. 1986, Richardson, Texas: Society of Petroleum Engineers. p. 141-142.

[50] Chakraborty, G., *A note on methods for analysis of flow through microchannels.* International Journal of Heat and Mass Transfer, 2008. **51**: p. 4583-4588.

[51] Madlener, K., Frey, B., Ciezki, H. K., *Generalized Reynolds Number for Non-Newtonian Fluids.* Progress in Propulsion Physics, 2009. **1**: p. 237-250.

[52] Rye, O.J., *Statistical Analysis of Rheological characterization of Water-based Drilling Fluids*, in *Petroleum Geoscience and Engineering*. 2017, Norwegian University of Science and Technology.

[53] Hassiba, K.J., Amani, M., *The Effect of Salinity on the Rheological Properties of Water Based Mud under High Pressures and High Temperatures for Drilling Offshore and Deep Wells.* Earth Science Research, 2012. **2**(1).

[54] Hassiba, K.J., Amani, M., *The Effect of Salinity on the Rheological Properties of Water Based Mud under High Pressures and High Temperatures for Drilling Offshore and Deep Wells.* Earth Science Research, 2012. **2**(1).

[55] Moller, P., Fall, A., Chikkadi, V., Derks, D., Bonn, D., *An attempt to categorize yield stress fluid behavior.* Phil. Trans. R. Soc. A, 2009. **367**: p. 5139-5155.

[56] Dubash, N., Frigaard, I. A., *Propagation and stopping of air bubbles in Carbopol solutions.* J. Non-Newtonian Fluid Mech., 2007. **142**: p. 123-134.

[57] Kelessidis, V.C., Hatzistamou, V., *Preparation Methodology and Rheological Properties of Yield Pseudo Plastic Transparent Fluids.* Journal of Dispersion Science and Technology, 2011. **32**(3): p. 380-388.

[58] Nelson, E.B. and D. Guillot, *Well cementing*. 2nd ed. 2006, Sugar Land, Texas: Schlumberger. p. 129-130.

[59] Rashaida, A.A., *Flow of a Non-Newtonian Bingham Plastic Fluid Over a Rotating Disk*, in *Department of Mechanical Engineering*. 2005, University of Saskatchewan. p. 81.

[60] Berntsen, K., Simonsen, H., *Investigation and Implementation of Different Non-Newtonian Rheology Models in a Steady-State Model for One-Phase Flow*, in *Department of Petroleum Engineering*. 2015, University of Stavanger.